NASA/TP—2004-212903

A Method of Estimating Low Turbulence Levels in Near Real Time Using Laser Anemometry

Louis J. Goldman and Richard G. Seasholtz
Glenn Research Center, Cleveland, Ohio

September 2004

The NASA STI Program Office . . . in Profile

Since its founding, NASA has been dedicated to the advancement of aeronautics and space science. The NASA Scientific and Technical Information (STI) Program Office plays a key part in helping NASA maintain this important role.

The NASA STI Program Office is operated by Langley Research Center, the Lead Center for NASA's scientific and technical information. The NASA STI Program Office provides access to the NASA STI Database, the largest collection of aeronautical and space science STI in the world. The Program Office is also NASA's institutional mechanism for disseminating the results of its research and development activities. These results are published by NASA in the NASA STI Report Series, which includes the following report types:

- TECHNICAL PUBLICATION. Reports of completed research or a major significant phase of research that present the results of NASA programs and include extensive data or theoretical analysis. Includes compilations of significant scientific and technical data and information deemed to be of continuing reference value. NASA's counterpart of peer-reviewed formal professional papers but has less stringent limitations on manuscript length and extent of graphic presentations.

- TECHNICAL MEMORANDUM. Scientific and technical findings that are preliminary or of specialized interest, e.g., quick release reports, working papers, and bibliographies that contain minimal annotation. Does not contain extensive analysis.

- CONTRACTOR REPORT. Scientific and technical findings by NASA-sponsored contractors and grantees.

- CONFERENCE PUBLICATION. Collected papers from scientific and technical conferences, symposia, seminars, or other meetings sponsored or cosponsored by NASA.

- SPECIAL PUBLICATION. Scientific, technical, or historical information from NASA programs, projects, and missions, often concerned with subjects having substantial public interest.

- TECHNICAL TRANSLATION. English-language translations of foreign scientific and technical material pertinent to NASA's mission.

Specialized services that complement the STI Program Office's diverse offerings include creating custom thesauri, building customized databases, organizing and publishing research results . . . even providing videos.

For more information about the NASA STI Program Office, see the following:

- Access the NASA STI Program Home Page at ***http://www.sti.nasa.gov***

- E-mail your question via the Internet to help@sti.nasa.gov

- Fax your question to the NASA Access Help Desk at 301–621–0134

- Telephone the NASA Access Help Desk at 301–621–0390

- Write to:
  NASA Access Help Desk
  NASA Center for AeroSpace Information
  7121 Standard Drive
  Hanover, MD 21076

NASA/TP—2004-212903

A Method of Estimating Low Turbulence Levels in Near Real Time Using Laser Anemometry

Louis J. Goldman and Richard G. Seasholtz
Glenn Research Center, Cleveland, Ohio

National Aeronautics and
Space Administration

Glenn Research Center

September 2004

Acknowledgments

The authors wish to thank Kristie Ann Elam of Akima Corporation for writing the subroutine to read Acqiris binary data files; Gerald J. VanFossen (retired) of NASA Glenn Research Center for the cascade inlet hot-wire measurements; and Robert J. Boyle of NASA Glenn Research Center for the nozzle exit hot-wire measurement.

This work was sponsored by the Low Emissions Alternative Power Project of the Vehicle Systems Program at the NASA Glenn Research Center.

Available from

NASA Center for Aerospace Information
7121 Standard Drive
Hanover, MD 21076

National Technical Information Service
5285 Port Royal Road
Springfield, VA 22100

Available electronically at http://gltrs.grc.nasa.gov

Method of Estimating Low Turbulence Levels in Near Real Time Using Laser Anemometry

Louis J. Goldman and Richard G. Seasholtz
National Aeronautics and Space Administration
Glenn Research Center
Cleveland, Ohio 44135

Summary

A laser anemometer (LA) system was used to make two independent measurements of the fringe crossing frequency (proportional to the flow velocity) of seed particles passing through the probe volume. The light scattered by the seed particle produces a Doppler signal or burst that is captured by high-speed digitizing boards. The purpose of the two independent measurements was to attempt to reduce or eliminate the contribution of photodetector shot noise on the frequency determination and subsequently on the turbulence estimate. This purpose was accomplished by cross-correlating the two measured frequencies and assuming that the shot noise terms were independent. Measurements were obtained at the inlet of an annular cascade operating at transonic flow conditions (the cascade inlet flow being subsonic) and at the exit of a hot-wire flow calibration nozzle (set to be at similar flow level as cascade tests). One observation made relatively early on was that the quality of the individual bursts varied widely, ranging from very bad to very good. The thinking was that without eliminating the "bad" bursts, acceptable turbulence estimates would not be possible.

The first step leading to a successful turbulence estimation method was to determine the "good" local peaks of the Doppler burst and to reject any bursts with obviously false peaks. Once this determination was made, Doppler burst symmetry conditions based on these local peak determinations were then used to reject bursts without the selected symmetry requirements. Twelve burst "goodness" criteria were identified and used to reject the bad bursts. Then, acceptable turbulence estimates were made. For the good bursts, a Fast Fourier Transform (FFT) was used to calculate the power spectrum of the Doppler signal. A nonlinear least-squares fit of the power spectrum to a Gaussian function with noise resulted in the determination of the Doppler frequency.

The cross-correlated turbulence estimates were always lower than the noncorrelated turbulence estimates, which demonstrated that this method reduced or eliminated the effect of photodetector shot noise on the turbulence measurement. The cross-correlated turbulence agreed reasonably well with independent hot-wire measurements, with the cascade and nozzle turbulences being about 3/4 and 1/4 percent, respectively.

The turbulence estimation procedure described herein can be used to give near-real-time results. For example, a typical data subset of 3000 bursts requires about 30 s to process. A Dell Precision 420 computer with dual Pentium III processors (800 MHz) was used to process the data, so the execution times might be different for other computer systems.

Introduction

Turbulence parameters are important quantities that need to be measured or estimated in many turbomachinery flow situations. A major use of this information is in viscous computational fluid dynamic (CFD) computer codes where they provide one important upstream flow boundary condition. Accurate turbulence information is required to accurately calculate the losses occurring in turbomachinery. The CFD results might then be used to design more efficient turbomachinery components. In addition, the CFD calculations may reveal important flow physics information, such as shock formation or boundary layer separation.

The non-intrusive determination of turbulence parameters using laser anemometry is a natural byproduct of a typical data acquisition where the mean velocity estimate is based on many individual velocity

measurements. It is then easy to calculate the turbulence intensity from the square root of the sum of the square of the differences of the individual velocities from the mean velocity.

Unfortunately, the accuracy of the turbulence estimate from laser anemometer (LA) measurements is questionable. The problem is that a few bad bursts can severely bias the turbulence estimate. This bias is apparent when LA turbulence estimates are compared with hot-wire results. An example of this is the author's work (ref. 1), which reported that the turbulence intensity upstream of a stator vane measured using LA averaged about 3 percent. Subsequent measurement with a hot-wire probe yielded values less than 1 percent. Even more striking is the lack of LA turbulence measurements less than about 1/2 to 1 percent (ref. 2) using commercial counters or frequency domain processors. With the advent of high-speed digitizers capable of capturing individual Doppler bursts, the problem was immediately clear; there was a large variation in the quality of the individual bursts.

It is easy to hypothesize that all that needs to be done to obtain accurate turbulence estimates from individual LA measurements is to just remove the bad bursts. Unfortunately, how to do this is not obvious. Even the old standby of discarding bad bursts based on low signal-to-noise ratio (SNR) was not sufficient for the cascade inlet flow measurements (ref. 1) discussed previously. An attempt of the present study to find a single universal rejection criterion was also unsuccessful. What eventually worked herein was a battery of rejection criteria (12 in all) that were partly based on the properties of how a theoretical Doppler burst should behave. Also useful was a technique (ref. 3) used to eliminate photomultiplier tube (PMT) shot noise by making two independent measurements of the same seed particle velocity. This permits cross-correlation of the two measurements to remove or reduce the PMT shot noise.

This report describes the rejection criteria used to eliminate the bad bursts and also addresses the cross-correlation procedure to reduce the effect of PMT shot noise. The LA turbulence estimated by this procedure is then compared with the hot-wire results for the cascade inlet flow alluded to previously (ref. 1). In addition, LA measurements obtained at the exit of a flow calibration nozzle (low turbulence level) are compared with hot-wire results.

Appendix A contains the list of symbols used herein; appendix B describes the method of estimating the signal-to-noise ratio from a given seed particle Doppler burst; and appendix C describes the method of estimating the turbulence from cross-correlating two independent frequency measurements of the same seed particle passing through the probe volume.

Apparatus and Procedures

Annular Cascade Facility

A photograph and schematic of the stator vane annular cascade facility are shown in figures 1 and 2, respectively. During operation of the cascade, atmospheric air is drawn through the inlet section, the vanes, and a dump-diffusing exit section and is then exhausted through the laboratory exhaust system. Before entering the exhaust system, the flow passes through a flow-straightening section that removes the swirl created by the stator vanes.

Inlet section.—The inlet, consisting of a bellmouth and a straight section, was designed to accelerate the flow to uniform axial-flow conditions at the vane inlet. The bellmouth profile and coordinates are presented in reference 4.

Test section.—The test section consisted of a full-annular ring of 26 vanes. A cutout in the outer cascade housing provided access for the laser beams. The vanes in this region were machined to the vane tip radius so that the window would fit flush with the tip endwall. The window is described in the next section.

The stator vane geometry and coordinates are presented in reference 1. The untwisted vanes, of constant profile from hub to tip, had an axial chord of 35.56 mm and a vane height of 38.10 mm. These properties resulted in a vane aspect ratio and solidity at the mean radius (based on axial chord) of 1.07 and 0.63, respectively. The vanes used herein represented a 0.771-scale model of a typical energy efficient engine (E^3) stator (ref. 1).

Window.—Optical access for the laser beams was provided by a cutout in the cascade housing (fig. 1) that extended approximately two axial chords upstream and one axial chord downstream of the vane passage. The window was manufactured using standard lens techniques and was ground from 3.175-mm-thick optical glass. The high-quality window lens was necessary because of the small laser probe volume (PV) of 50 μm employed in the optical design and the possibility that the beams would uncross on passing through the window. A silicone rubber sealing material

was used to seal the window to the cascade housing and seal the vane tips to the window. The window covered about 36° in the circumferential direction and had an axial length of 140 mm.

Flow Calibration Nozzle

A DISA-type 55D45 nozzle unit designed for the flow calibration of hot wires was used to provide a low turbulence flow. The flow calibration nozzle consisted of a straight section and a convergent section with an exit area of 120 mm^2. The nozzle was designed to provide an exit flow of 40 m/s but was operated herein at about 50 m/s, which is similar to the cascade inlet flow condition. Filters upstream of the nozzle were used to make the flow laminar in the nozzle section. A photograph of the calibration nozzle and the laser anemometer system is shown in figure 3. During operation of the flow calibration facility, pressured air entered the nozzle inlet section, passed through a wire mesh filter, and exhausted to the atmosphere.

Laser Anemometer System

A modification of the cascade laser anemometer system of reference 1 was used herein and is shown in figure 4. The main differences between the present configuration and that described in reference 1 are the addition of a beam splitter to divide the scattered light into two equal-intensity beams and the inclusion of a second photomultiplier tube to measure the light from the second scattering beam. The above modifications to the laser optical system allowed two independent frequency measurements to be made from the same seed particle passing through the probe volume. These two frequency measurements were then cross-correlated to reduce the shot noise contribution to the calculated velocity (see appendix C for details). The optical system modification and cross-correlation calculation procedure were first reported in reference 3. For the flow calibration nozzle LA system, there was no window, so no cylindrical correction lens C1 was needed. Also, fewer mirrors were used and a single focusing lens provided the same probe-volume beam diameter and number of fringes as in the cascade LA configuration. In addition, a TSI Inc., beam splitter was used in the calibration nozzle setup. The probe volume in both systems had a $1/e^2$ diameter of about 50 μm and fringe spacing of 5.2 μm, resulting in bursts with about 9 cycles.

An organic aerosol (Rosco fog/smoke fluid) was used as the seeding material for the tests. The fluid was atomized with a commercial TSI Inc., six-jet aerosol generator. The aerosol for the cascade tests was passed through a centrifugal separator to remove any large droplets before being injected through a 6-mm-diameter tube into the flow at the bellmouth inlet. The seed particle size distribution was measured previously (ref. 1) and ranged mostly between 0.3 to 0.6 μm in diameter. For the calibration nozzle, the seed was injected upstream of a fine wire mesh filter at the nozzle inlet. This filter apparently removed many large seed particles because initial tests conducted by injecting the seed particles downstream of the wire mesh produced poor signal quality. The fine wire mesh had to be cleaned frequently because condensation of the seed aerosol clogged the wire mesh and decreased the seeding rate.

Test Procedures

Cascade flow conditions.—The test conditions in the cascade were set by controlling the pressure ratio across the vane row with two throttle valves located in the exhaust system. A hub static tap located downstream of the test section (at station M, fig.2) was used to set this pressure ratio. For the results presented herein, the ratio of the exit hub static pressure to the inlet total pressure was set to 0.491. This flow condition is the same as that used in reference 1. Laser anemometer measurements were obtained one axial chord upstream of the vane leading edge (station 1) at the mean radius where the velocity was about 55 m/s.

Calibration nozzle conditions.—The test conditions in the nozzle were set by controlling the inlet pressure. The pressure ratio across the nozzle was set so that the nozzle exit flow velocity (50 m/s) would be similar to the cascade inlet flow velocity level. A static tap located in the upstream nozzle straight section was used to measure and set the inlet pressure. Measurements were obtained at the center of the nozzle as close to the nozzle exit as was practical.

Data acquisition.—A Dell Precision 420 computer with dual Pentium III processors operating at 800 MHz was used to acquire and process the data. Two Acqiris DP105 digitizer boards (ref. 5) were installed in the computer. Each board was equipped with extra memory to allow 2 million points of storage. The signals from the photomultiplier tubes were directly input to the digitizing boards without preconditioning. Although the digitizing boards were

able to acquire data at rates up to 500 million samples per second (MS/s), a 100-MS/s sampling rate was used for this investigation. Data were obtained in sequence acquisition mode, which allows the capture and storage of consecutive Doppler bursts with each burst requiring its own individual trigger. For laser anemometer measurements in which the arrival of seed particles to the probe volume is random, this data acquisition mode is ideal because it eliminates any dead time between particle arrivals. The acquisition boards also permit a pretrigger delay of 0 to 100 percent to be applied to the trigger position. A pretrigger value of 50 percent was used, which means that half the measurement points saved are before the burst was triggered. This is possible because the boards are always taking data and saving it to onboard memory so that when a triggered event occurs, the data are already there in memory and just need to be saved. If a triggering event does not occur for some time, the older data in memory are replaced by more recent data; thus, there is always enough newer data to provide the 50-percent pretrigger values specified.

Method

A method for estimating low turbulence levels using laser anemometry rejects bad bursts by defining goodness criteria for the Doppler burst local peaks and symmetry conditions. Only the good bursts that remain are processed further. Fast Fourier Transforms (FFTs) are used to obtain the power spectrum of each burst in the frequency domain, and a nonlinear least-squares fit to a Gaussian function gives an estimate of the Doppler frequency. In addition, noise due to photomultiplier shot in the Doppler signal can be minimized by making two independent measurements of the same seed particle frequency (or velocity). Cross-correlation of the two measurements is then used to obtain the frequency and turbulence estimates (ref. 3). Near-real-time estimates are also possible if a subset of the burst data is employed and bursts are eliminated as soon as one goodness criterion fails to be met. This method will be explained in the following section.

Dual-Channel Burst Coincidence Determination

As discussed in the Test Procedures section, two digitizer boards were set up to provide two independent measurements of the same seed particle frequency (or velocity, which is assumed to be the flow velocity). All user-controlled parameters (e.g., trigger level, voltage range, digitizing rate) were set the same for each board. However, slight differences in the two photomultiplier tubes and their corresponding optics can result in a seed particle triggering one of the digitizer boards but not the other. Since both boards are controlled by their own internal clocks, it cannot be assumed that the first burst from board 1 (channel 1, *Ch*1) will correspond to the same seed particle as the first burst recorded by board 2 (channel 2, *Ch*2). If they did correspond, the two bursts would be considered coincident (i.e., resulting from the same seed particle). What is true is that the trigger time difference *delta trig*1 (see fig. 5) between two coincident bursts of *Ch*1 will be equal to the trigger time difference *delta trig*2 between the two corresponding coincident bursts of *Ch*2, within some tolerance value. Thus, for the first coincidence determination, actually two burst coincidences must be established; call these coinc1 and coinc2. The third coincidence, coinc3, is found using the last found coincidence, coinc2. All subsequent coincidences are found in a similar manner. Figure 5 is a schematic of two Doppler burst records in which bursts 1 and 3 of *Ch*1 are coincident with bursts 1 and 2 of *Ch*2. These then correspond to coinc1 and coinc2. The third coincidence, coinc3, corresponds to burst 4 of *Ch*1 and burst 3 of *Ch*2. Note that burst 1 of *Ch*1 and burst 1 of *Ch*2 are coincident in figure 5, but as explained above, this is not a requirement of the coincidence procedure.

To set the tolerance value, the following considerations were made. First, the LA probe-volume width (50 μm) and estimated inlet flow velocity (55 m/s) result in a seed particle residence time in the PV of about 1 μs, or 10^6 ps. This tolerance limit would be reasonable if the trigger time measurement had zero error. The time accuracy, however, is quoted as ±25 ppm times the time period. Because the time period was selected as the difference between adjacent trigger times, a ±50 ppm times the time period was used. The tolerance limit was therefore set to 10^6 ps plus the time measurement accuracy as given above. Note that the time measurement accuracy is not a constant because the time difference between adjacent trigger times is not constant. Usually, the time measurement accuracy is much less than a seed particle residence time of 10^6 ps, averaging about 0.04×10^6 ps. However, if data dropout occurs (when the seed particles do not pass through the PV for awhile), the time measurement accuracy will be much greater than the seed particle residence time of 10^6 ps. For this

situation, if the time measurement accuracy were not added to the tolerance limit, the coincidence procedure would prematurely stop at the data dropout point.

Because of the importance of ensuring that the first two burst coincidences are correct, the tolerance limit for this part of the calculation was decreased an order of magnitude to 10^5 ps plus the time measurement accuracy as given above. The search criteria for the first burst coincidence allowed for any of the first 10 bursts to be coincident, with the second burst coincidence being up to 10 bursts away from the first. It was not required that *Ch*1 and *Ch*2 bursts be the same burst number. This procedure sometimes found more than one set of burst coincidences that satisfied the tolerance limit. The burst coincidence with the minimum trigger time difference was saved and other possible burst coincidences were discarded.

For subsequent burst coincidences, the search criterion was increased to 500 bursts away from the last burst coincidence. This increase was also made to prevent the coincidence calculation procedure from aborting prematurely. Typically, coincident burst pairs are only a few bursts away from the previous coincident burst pairs and this then aborts the search procedure.

Typical results of the coincidence determinations are shown in figures 6 and 7. Figure 6 shows the first signals in the data set that were coincident, and figure 7 shows the last signals that were coincident. In each figure, the top two plots show the full data set of 1000 measurements, whereas the bottom two plots show the details of the actual triggered burst in a windowed (256 points) portion of the measurement set. What are also captured occasionally are other seed particle bursts, as seen in the far right of the top plots of figures 6 and 7. Although these are unwanted features and are not used in the frequency determination, they do provide more convincing confirmation of the coincidence procedure in that similar features appear in both the *Ch*1 and *Ch*2 data.

A typical variation of trigger times versus burst number is shown in figure 8 for the same data subset used in figures 6 and 7. Note that the data rate (burst number/trigger time) for *Ch*1 is slightly greater than that for *Ch*2. The greater rate is caused by differences in the properties of the two PMTs and slight differences in the optical adjustments of the two channels. The result of these differences is that *Ch*1 finishes taking its required 1500 bursts before *Ch*2. Thus, none of the subsequent burst measurements of *Ch*2 can be coincident with those of *Ch*1, since *Ch*1 has finished taking data. For this data subset, the number of burst coincidences was determined to be 1153. A large data dropout (a near vertical line) also occurs around burst number 500 and many smaller dropouts are also observed.

Determination of Doppler Burst Local Peak Minimums and Maximums

Typical Doppler bursts shown in figures 6 and 7 were characterized by multiple local peak minimums and maximums. As is well known, these local peaks are the result of the seed particle passing through the fringes within the probe volume. To estimate the frequency in the frequency domain, knowledge of the local peak minimums and maximums is not required. However, this information is used to determine the goodness of the bursts and thus to permit the rejection of bad bursts. Only the windowed or triggering portion of the burst, typically of 256 points (bottom plots of figs. 6 and 7), was used for the local peak determination.

Each of the local peaks is characterized by a change in sign of the slope of the signal voltage versus measurement index (which is proportional to time). What is not so obvious is that peaks may have two adjacent points with the same magnitude, resulting in a zero slope. This occurs because of the digitizer discrete nature, caused by the 8-bit resolution and the typical ±1-percent accuracy. Even a theoretical Doppler burst sampled at delta times similar to the experimental value can result in a zero or near-zero-slope peak value (see fig. 9, peak 1). For the peak determination, five adjacent data points were used, resulting in four slopes that were normalized to give a value of −1, 0, or 1. This quadruplet of slope values was tested to determine the local minimum peaks. If any of the five adjacent points was below the trigger level (typically −30 mV), the slope quadruplet was calculated and tested. The starting measurement point for the next quadruplet was incremented by 1, so that the next data set contained four points that were in the previous calculated quadruplet. Tests were then needed to ensure that the same good peak was only determined once. This procedure continued until all the five adjacent points were above the trigger level.

An implicit assumption made herein is that the data sampling rate is high enough to provide the required five data points to adequately define the peaks. A typical sampling rate of 100 MS/s was employed for these tests, and as seen from figures 6 and 7, this

requirement was met. Also, sampling at a higher rate (e.g., 200 MS/s) is not necessarily better because it can lead to more jumpiness in the burst capture and result in rejection due to failure of the peak goodness tests. In these cases, a running average of the burst measurements (e.g., two adjacent measurements) can be used to smooth out the bursts before doing the peak determination tests.

Eleven slope quadruplets were considered to be good minimum peaks:

1. \ / (–1, –1, 1, 1)
   \/

2. \ _ (–1, –1, 1, 0)
   \/

3. _ / (0, –1, 1, 1)
   \/

4. / (–1, 1, 1, 1)
   /
   \/

5. \ (–1, –1, –1, 1)
   \
   \/

6. _ (–1, 1, 1, 0)
   /
   \/

7. _ (0,–1, –1, 1)
   \
   \/

8. _/ (–1, 1, 0, 1)
   \/

9. _ (–1, 0, –1, 1)
   \/

10. \ (–1, –1, 0, 1)
    _/

11. / (–1, 0, 1, 1)
    _/

Nine slope quadruplets were considered bad in that they did not correspond to valid peaks. However, only number 1 was used to reject bursts because it could result in two false adjacent peaks being determined. Numbers 2 to 8 were considered bad because they had two or more zero slopes. Test numbers 3, 4, and 6 could result in a peak being determined for that quadruplet depending on the next adjacent point, but only one valid peak. For example, bad peak number 3 could result in a good peak number 8 if the next data point is larger than the last (or fifth point of the slope quadruplet). Numbers 2, 5, and 7 to 9 could not result in a peak determination (with an adjacent point) using the previous 11 tests. It should be noted that because tests 2 to 9 did not result in an outright rejection, it did not mean that bursts containing any of these peaks were used in the turbulence calculation procedure. What usually occurs is that these bursts are rejected by one or more of the symmetry goodness criteria (discussed in the section Goodness Characterization of Doppler Burst) since one or more of these peaks is not considered a valid peak. The nine slope quadruplets are

1. \/ (–1, 1, –1, 1)

2. _ _/ (–1, 0, 0, 1)

3. _ _ (0, –1, 1, 0)
   \/

4. _ _ (0, 0, –1, 1)
   \/

5. _ _ (–1, 1, 0, 0)
   \/

6. _ (0, –1, 0, 1)
   _/

7. _ (–1, 0, 1, 0)
   _/

8. _ _ _ (–1, 0, 0, 0)

9. _ _ _/ (0, 0, 0, 1)

The reader should also note that instead of five adjacent points, four adjacent data points and three slopes could also be used to determine the local peak minimums. This procedure was tried initially but did not provide results as good as the five adjacent data point procedure.

After the local minimum peaks were determined, the local maximum peaks were obtained in a similar

manner with the slopes being reversed. That is, a negative slope (−1) for the minimums becomes a positive slope (1) for the maximums. And a positive slope (1) for the minimums becomes a negative slope (−1) for the maximums. For example, the first good local minimum peak quadruplet of (−1,−1,1,1) listed above results in a good local maximum peak with a quadruplet of (1,1,−1,−1). The trigger level test was not used for the determinations of the maximums because the values of the local maximums would have been near zero for a high visibility burst, well above the usual trigger level typically used herein. The test for peak maximums started at the first minimum peak location and continued to the last minimum peak location plus an estimate of the number of points between corresponding minimum and maximum locations. Similar bad peak maximums can be defined as in the nine bad minimum peaks in the previous list; however, as defined for the minimums, only the first test is used to reject bursts.

The local peak minimums are additionally tested to determine the leftmost minimum value *pkmin*(*nl*) and the corresponding measurement index *nl* (fig. 9). The local peak minimums are then tested again to determine if there is another peak with the same minimum value. This peak is designated the rightmost minimum value *pkmin*(*nr*) with a corresponding measurement index *nr*. These values are saved for future use in the Doppler burst goodness criteria discussed in the next section. The number of minimum and maximum peaks is also checked to ensure that neither is zero. A zero-slope peak value can occur for a weak signal that just triggers the digitizing board although the peak is not considered a good peak, as defined above. These bursts, if they occur, are rejected. The final peak goodness test searches the burst for any data point that is less than *pkmin*(*nl*). This situation can occur when a portion of a second (larger particle) burst is captured within the windowed portion of the measurement record or the minimum value does not correspond to a good peak. This type of burst measurement gives a very poor estimate of the Doppler frequency and thus a highly biased turbulence estimate. Bursts of this type are also rejected.

Goodness Characterization of Doppler Burst

In the previous section, the local peak determinations included three peak characterizations considered to be bad: double-peak minimums or maximums; zero *minpks* or *maxpks* value; *pkmin*(*nl*) no minimum value within the windowed signal. Bursts having any one of these characterizations are rejected to eliminate many that are questionable. However, many bad bursts are still left. Therefore, a theoretical Doppler burst (fig. 9) is employed to define the burst goodness criteria. The data points in the figure closely represent the data sampling rate of 100 MS/s used in the experimental results. The basic characteristic of the theoretical Doppler burst is the symmetry about the single minimum peak (normalized magnitude value of −1). For the optical properties of the LA used herein, nine fringes are present in the probe volume (width corresponding to $1/e^2$-scattered-light-intensity points). The expectation is that a Doppler burst for this LA should have a maximum of nine local minimum and nine local maximum peaks. The Doppler burst symmetry and the theoretically expected nine local minimum and maximum peaks form the basis used to define the following goodness criteria:

1. *nl* = *nr*—only one peak minimum occurs

2. *minpks* = *maxpks*—same number of local minimum and maximum peaks found

3. *nl* = 2, 3, 4, or 5—if < 2, not enough information for good frequency estimate if > 5, too many peaks in burst (see 7 below)

4. If *nl* = 2, then *minpks* = 3—symmetry of burst peaks

5. If *nl* = 3, then *minpks* = 5—symmetry of burst peaks

6. If *nl* = 4, then *minpks* = 7—symmetry of burst peaks

7. If *nl* = 5, then *minpks* = 9—symmetry of burst peaks

8. *pkmin*(*m*) trend—values of peak minimums should decrease from leftmost local peak *pkmin*(1) to *pkmin*(*nl*), then increase to rightmost local peak *pkmin*(*minpks*)

9. pedestal(*m*) trend—1/2[*pkmin*(*m*) + *pkmax*(*m*)] values should follow similar trend as 8

These nine goodness criteria, taken together with the three peak badness criteria, place a very restrictive test on the experimental data sets in that 90 to 95 percent of the bursts are rejected. However, what remains is generally a very good subset of the data. Bursts that are rejected usually have more than one failed test. The number of failed tests (number of bad burst rejections) is saved in the variable *n*bad and this value can be used as another goodness criterion if desired. For example, although an *n*bad value of 1 probably corresponds to a reasonably good burst, for a near-real-time turbulence estimate, a burst with only one rejection (*n*bad = 1) is discarded and no further tests are performed on this burst. This rejection obviously decreases the time necessary to process the burst data.

Another implied test is that both coincident bursts must pass all the goodness criteria. If either burst fails, then both bursts must be rejected. The reason is that two independent measurements are needed to cross-correlate the two frequencies determined for the same seed particle.

Note that all the rejection tests defined herein are independent of frequency, as they should be.

Least-Squares Estimate of Flow Frequency in Frequency Domain

The flow frequency is estimated using a FFT to calculate the power spectra for the Doppler burst. An International Mathematical and Statistical Library (IMSL) subroutine is used to provide the FFT. Generally, only the good bursts that pass the previous goodness tests are processed, unless *n*bad is set to a very high value so as not to reject any coincident bursts. A typical plot of power spectrum versus frequency is shown in figure 10 for a good burst. The large peak near zero frequency is the pedestal, or dc, value and is not of interest for the burst frequency estimate. The smaller peak at a frequency of about 10.5 MHz represents the Doppler portion of the power spectrum. A nonlinear least-squares calculation is used to obtain the Doppler frequency based on a theoretical model function, Gaussian plus noise, given by equation (1):

$$p = a3\,\mathrm{e}^{-0.5\left\{\left[(f-a1)/a2\right]^2\right\}} + a4 \qquad (1)$$

where p is the power spectral density; f is the frequency; the parameter $a1$ is the desired Doppler burst frequency or the location of the peak of the Gaussian function; $a2$ is the Gaussian function half-width; and $a3$ is the peak amplitude of the Gaussian function. The white noise term $a4$ is primarily due to the PMT shot noise. The nonlinear least-squares method is applied to data between lower and upper frequency limits f_l to f_u, respectively. These lower and upper frequency limits were set to 5 and 15 MHz, which corresponds to what would be set on a commercial LA counter measuring an expected frequency of 10 MHz. Nonlinear least-squares methods have been fully described in many references (including refs. 6 to 8).

Other simpler estimates of the Doppler frequency from the FFT are of course possible and were tried. For example, using the peak value of the Doppler signal led to large quantization-type errors because the difference in frequency values of adjacent measurement points is relatively large, about 0.4 MHz. Similarly, using three adjacent points about the peak and fitting to a parabola did not give significantly better frequency estimates.

Signal-to-Noise-Ratio Approximation and Turbulence Estimate

Signal-to-noise-ratio approximation.—As discussed in the Introduction, the SNR has long been used to characterize the goodness of the laser measurements. However, a battery of goodness tests is proposed herein to provide a better characterization. Although the SNR is still useful in demonstrating how the turbulence estimate varies with this parameter, a new, fast method of estimating the SNR value was developed by using the underlying ideas presented in reference 9. The main purpose of this reference was to estimate the SNR during the design phase of the LA system. Thus, the estimate was based mainly on the optical characteristics of the LA, the photodetector properties, and the particle size. Our purpose was different: we wanted to estimate the SNR for a given seed particle Doppler burst. The calculations were performed at the peak amplitude *pkmin*(*nl*), and only shot noise generated in the photodetector by light scattered from the seed particles was considered. Figure 11 gives the nomenclature for estimating the SNR from burst. From the procedure described in appendix B, the peak signal-to-noise ratio *SNR*(*nl*) is

$$SNR(nl) = c2\left[pkmin(nl) - pkmax(nl)\right]^2 \Big/ \left[pkmin(nl) + pkmax(nl)\right] \qquad (2)$$

where $c2$ is a constant. If $pkmax(nl) = 0$, the $SNR(nl)$ is

$$SNR(nl)_{maxV} = c2\,pkmin(nl) \qquad (3)$$

Equation (3) suggests that bursts with larger $pkmin(nl)$ values are better than bursts with smaller $pkmin(nl)$ values, since these bursts give larger SNR *maxV* values. The suggestion is that larger particles result in better bursts since they scatter more light and give larger $pkmin(nl)$ values. However, larger particles may not follow the flow fluctuations as well as smaller particles, so turbulence estimates based on SNR may not be the best criterion to use. Therefore, a normalized $SNR(nl)$ was defined as

$$SNR(nl)_{\text{normalized}} = \frac{SNR(nl)}{SNR(nl)_{maxV}}$$

$$SNR(nl)_{\text{normalized}} = \frac{\left[pkmin(nl) - pkmax(nl)\right]^2}{pkmin(nl)\left[pkmin(nl) + pkmax(nl)\right]} \qquad (4)$$

This definition of a normalized SNR allows smaller particles to compete with larger particles on an equal basis. Note that if $pkmax(nl) = 0$, $SNR(nl)_{\text{normalized}} = 1$, a very good burst. However, if $pkmax(nl) = pkmin(nl)$, $SNR(nl)_{\text{normalized}} = 0$, a very bad burst.

Turbulence estimate.—The turbulence is estimated from the cross-correlation of all the coincident burst frequency measurements in which two independent frequency measurements are obtained from the same seed particle. As described in reference 3, this procedure should remove or reduce photodetector shot noise. The calculation method is described in appendix C. The measured frequency containing shot noise $f_{i,j,\text{noise}}$ can be written as the sum of the true frequency $f_{i,j}$ and a shot noise term $e_{i,j,\text{noise}}$:

$$f_{i,j,\text{noise}} = f_{i,j} + e_{i,j,\text{noise}}$$
$$i = 1,2\ (Ch1, Ch2)$$
$$j = 1 - n \qquad (5)$$

where n is the number of measurements. The shot noise terms are considered to be uncorrelated to frequency or themselves.

From appendix C, the average frequency $\overline{f_{1+2}}$ is

$$\overline{f_{1+2}} = \frac{1}{2}\left(\overline{f_1} + \overline{f_2}\right)$$

$$\overline{f_1} = \frac{1}{n}\sum_{j=1}^{n} f_{1,j} \quad \text{and} \quad \overline{f_2} = \frac{1}{n}\sum_{j=1}^{n} f_{2,j} \qquad (6)$$

and the cross-correlated turbulence Tu_{12} (in percent) is

$$Tu_{12} = 100.0\frac{\sqrt{\overline{f_1 f_2} - \overline{f_{1+2}}^2}}{\overline{f_{1+2}}}$$

$$\overline{f_1 f_2} = \frac{1}{n}\sum_{j=1}^{n} f_{1,j} f_{2,j} \qquad (7)$$

The average frequency $\overline{f_{1+2}}$ and the cross-correlated turbulence Tu_{12} are independent of photodetector shot noise. However, for single-channel measurements (only one digitizer board), the turbulence estimate is affected by the shot noise term being larger than the true turbulence. See appendix C for details.

Near-Real-Time Results

The turbulence estimation method described in the last section can be used to give near-real-time estimates. To obtain the fastest execution time, the program can be set up to reject a burst as soon as one of the burst peak or goodness criterion fails. For a typical data subset of 3000 bursts, the program requires about 30 s to execute. This time is for two normalized signal-to-noise ratios, one being zero and the other being user defined (e.g., 0.4). A Dell Precision 420 computer with dual Pentium III processors (800 MHz) was used to process the data; the execution times might be different for other systems.

Results and Discussion

Good and Bad Bursts in Cascade Inlet Flow

The first and last coincidences for a cascade inlet data set were shown previously in figures 6 and 7, respectively. Both of these burst coincidences were rejected by the peak and burst goodness battery of tests

discussed in the sections Determination of Doppler Burst Local Peak Minimums and Maximums and Goodness Characterization of Doppler Burst. Rejecting the first burst coincident pair is obviously not a great loss since it is a low-visibility burst with little Doppler information. However, the last coincident pair, at first glance, looks fairly good. Closer inspection shows that the local minimum peak at a measurement index of about 115 corresponds to what was previously defined at a bad *minpks*2 (two adjacent zero-slope values). Therefore, although this burst is not rejected outright, this peak minimum is not considered valid. The result, then, is a failure of a burst symmetry condition.

The first coincident pair that passed all the peak and burst goodness tests is shown in figure 12. For this data set, the first 21 coincident pairs were rejected for one reason or another. The last coincident pair that passed all rejection tests is shown in figure 13. In this case, the last 18 coincident pairs were rejected. The accepted bursts of figures 12 and 13 look good. The near-zero-level noise in figure 13 could be better and exhibits a possible ac component. The cause could be electrical noise picked up in the approximate 50 ft of cable connecting the photomultiplier tubes to the computer in the control room. This noise is discussed further in the section Calibration of Nozzle Exit Flow results.

Two other examples of coincident bursts that were rejected are shown in figures 14 and 15. The example in figure 14 is of a burst (*Ch*1) containing a data point (last point) that has a lower value than the minimum peak value. Apparently, two other seed particles have been captured after the triggering particle. The windowing of the 1000-point record for the *Ch*1 burst happens to end before the last peak is fully defined. Even though this situation does not occur for the *Ch*2 burst, it would be rejected for having too many minimum peaks. The example in figure 15 is a burst that has two equal peak minimums (*nl* not equal to *nr*). Also, the capture of multiple seed particles results in the determination of too many peaks.

Figure 16 shows a coincident burst pair that passed all the rejection criteria. However, because these bursts are low visibility (less than 0.1), they are not considered as good as those in figures 11 and 12. Usually, low-visibility bursts, such as shown in figure 16, do not pass the entire peak and burst goodness tests and are rejected. Bursts similar to those of figure 16 could be rejected by accepting only bursts with good normalized SNRs, that is, greater than 0.4 or 0.5.

Turbulence and Frequency Estimates for Cascade Inlet Flow

The turbulence, frequency, and number of good measurements are shown in figures 17 to 20 for two cascade inlet flow data sets as a function of normalized SNR. Results are shown for *n*bad = 0, which means that all coincident bursts of *Ch*1 and *Ch*2 pass all the rejection criteria discussed previously. Each data set contains 9000 *Ch*1 and 9000 *Ch*2 bursts, but only 7056 and 6643 coincident pairs. In addition to the cross-correlated turbulence shown in figures 17 and 19, also shown are the noncorrelated turbulence calculated for the coincident *Ch*1 and *Ch*2 bursts (considered separate data sets for this calculation) and the combined data set of *Ch*1 and *Ch*2 bursts. As already explained, only the cross-correlated turbulence estimate can reduce or eliminate any errors caused by PMT shot noise. The calculated results support this conclusion in that the cross-correlated turbulence is always lower than the turbulence estimates of any of the noncorrelated measurement sets. Shown in figures 16 and 18 are three sets of hot-wire measurements made over a period of time. Any of the turbulence estimates give reasonable agreement with the hot-wire results. Also shown (figs. 17 and 19) are the Doppler frequencies that do not vary significantly with the method of estimating the frequency or with $SNR_{\text{normalized}}$. The Doppler frequencies shown (figs. 17 and 19) also do not vary significantly with the method of estimating the frequency (either single- or dual-frequency measurements). This agrees with the results of the theoretical analysis, showing that the frequency is independent of PMT shot noise (see appendix C). The frequency is also seen to not vary significantly with $SNR_{\text{normalized}}$.

The number of good measurement points is shown in figures 18 and 20 for the two corresponding data sets of figures 17 and 19. The number of good measurements represents the number of measurements remaining after $SNR_{\text{normalized}}$ is used as a rejection criterion. That is, for a $SNR_{\text{normalized}}$ value of 0.4, all coincident pairs that have a $SNR_{\text{normalized}}$ value less than 0.4 have been rejected. As $SNR_{\text{normalized}}$ increases, fewer good measurements remain and the uncertainty of the estimate increases, which may be the reason why the turbulence estimate drops off after a $SNR_{\text{normalized}}$ value greater than 0.6 for these data sets. Note that the number of measurements for *Ch*1 and *Ch*2 is equal to

the number for the cross-correlated data set. Even though the coincident data set has twice the number of bursts as *Ch*1 and *Ch*2 bursts (since it contains both these bursts), cross-correlating any coincident *Ch*1 and *Ch*2 pair gives only one data point. Thus, the number of coincident pairs is really the important parameter.

Figure 21 compares the cross-correlated turbulences for the two cascade inlet flow data sets. Turbulence uncertainty bars based on the number of measurements (eq. (22) in appendix C) are shown in the figure and overlap starting at a $SNR_{\text{normalized}}$ of 0.25 and greater. Also note that the uncertainty increases as $SNR_{\text{normalized}}$ increases because the number of good measurement points is decreasing. Not unexpectedly, the frequency estimate for the two data sets is essentially the same.

The effect of *n*bad on the cross-correlated turbulence is shown in figure 22. The previous results were shown for bursts with zero rejections; that is, all bursts passed all the peak and burst rejection tests and *n*bad = 0. As indicated previously, for every test failed, *n*bad was incremented by 1 and then this parameter could also be used as a rejection criterion. For example, a value of *n*bad = 1 indicates that bursts that fail only one peak and burst rejection criterion are retained. All others greater than 1 are rejected. For a large *n*bad value of 100, no bursts are rejected unless they fail the least-squares Gaussian fit to determine the Doppler frequency or have either zero *minpks* or *maxpks*. One feature not seen previously is that the cross-correlated turbulence is not nearly as constant with $SNR_{\text{normalized}}$ as with *n*bad = 0. This fact then makes it more difficult to decide what $SNR_{\text{normalized}}$ value to choose to get the correct turbulence. Also, keeping all the bursts (*n*bad = 100) gives poor results compared with the hot-wire measurements, except possibly at larger $SNR_{\text{normalized}}$ values. The frequency estimates do not vary greatly but show a slight decrease in frequency with $SNR_{\text{normalized}}$.

The effect of the number of bad burst rejections on the number of good measurements is shown in figure 23. Note that for all the coincident bursts (*n*bad = 100), the number of good measurements is about 7000 at $SNR_{\text{normalized}} = 0$. This number is close to the number of pairs of coincident bursts (7056) in this data set of 9000 *Ch*1 and *Ch*2 bursts.

Another way of looking at the effect of the number of bad burst rejections on the number of good measurements is seen in figure 24 where the individual burst Doppler frequencies are plotted as a function of $SNR_{\text{normalized}}$. Two cases are shown: *n*bad = 100 (all the coincident bursts are kept) and *n*bad = 0 (only the best bursts are kept). Actually, a restricted range of frequency is shown, and lower and higher individual frequencies occur for the results *n*bad = 100 (in magenta). What is obvious is that there are a lot of low $SNR_{\text{normalized}}$ data with a lot of frequency scatter. For *n*bad = 0 (in black), the frequency scatter is dramatically reduced and a lot of the low $SNR_{\text{normalized}}$ bursts have been rejected. Of course, this is why the turbulence is lower. It is important to note that the rejection tests used herein are all independent of frequency.

Turbulence and Frequency Estimates for Calibration Nozzle Exit Flow

The turbulence, frequency, and number of good measurements are shown in figures 25 to 28 for two data sets of the calibration nozzle exit flow as a function of $SNR_{\text{normalized}}$. Results are shown for *n*bad = 0, which means that all coincident bursts of *Ch*1 and *Ch*2 passed all the rejection criteria. Each data set contains 9000 channel 1 and 9000 channel 2 bursts, but only 5553 and 8079 coincident pairs. The cross-correlated turbulence is shown in figures 25 and 27. Also shown in these figures are the noncorrelated turbulence calculated for coincident *Ch*1 and *Ch*2 bursts (but considered separate data sets), in addition to the combined set of *Ch*1 and *Ch*2 bursts. As already explained, only the cross-correlated turbulence estimate can reduce or eliminate any errors caused by PMT shot noise, and these nozzle results also support this conclusion. In addition, the turbulence is almost constant with $SNR_{\text{normalized}}$. The reason for this is given below in the discussion of figures 26 and 28. Shown in figures 25 and 27 is a single hot-wire measurement. The cross-correlated turbulence estimates give reasonable agreement with the hot-wire results, which are almost identical to the data of figure 25. The noncorrelated turbulence estimates are higher than the hot-wire results, indicating that the cross-correlated method for low turbulence flows is more desirable. Also shown (figs. 25 and 27) is the Doppler frequency, which does not vary significantly with $SNR_{\text{normalized}}$ or with the method of estimating the frequency.

The number of good measurement points is shown in figures 26 and 28 for the two corresponding data sets of figures 25 and 27. As $SNR_{\text{normalized}}$ increases, the number of good measurements remains about the same, which is the reason why the turbulences (figs. 25 and 27) are almost constant. All bursts with a low

$SNR_{normalized}$ have been rejected by the peak and symmetry tests.

Figure 29 compares the cross-correlated turbulences for two data sets of nozzle exit flow. Turbulence uncertainty bars based on the number of measurements (eq. (22) of appendix C) are shown in the figure and do not overlap, which suggests that this simple uncertainty estimate based on the number of measurements is not adequate. Also note that the uncertainty is almost constant as $SNR_{normalized}$ increases because the number of good measurement points is also about constant. Not unexpectedly, the frequency estimate for the two data sets is essentially the same.

The effect of the number of bad burst rejections on the cross-correlated turbulence is shown in figure 30. The previous results were shown for coincident bursts with zero rejections; that is, all bursts passed all the peak and burst rejection tests and *n*bad = 0. As explained previously, for every test failed, *n*bad was incremented by 1 so that this parameter could also be used as a rejection criterion. For an *n*bad value of 100, no bursts are rejected unless they fail the least-squares Gaussian fit to determine the Doppler frequency or have zero number of *minpks* or *maxpks*. One feature also seen previously is that the cross-correlated turbulence is not as constant with $SNR_{normalized}$ as it was with *n*bad = 0, making it more difficult to decide what $SNR_{normalized}$ value to choose to get the correct turbulence. Also, keeping all the bursts (*nbad* = 100) gives poorer results compared with the single hot-wire measurement, except possibly at larger values of $SNR_{normalized}$. The frequency estimates do not vary with $SNR_{normalized}$.

The effect of the number of bad burst rejections on the number of good measurements is shown in figure 31. Note that for all the coincident bursts (*nbad* = 100), the number of good measurements is 5332 at $SNR_{normalized}$ = 0. This number is 221 fewer than the number of pairs of coincident bursts (5553) in the data set of 9000 *Ch*1 and *Ch*2 bursts. Of these, 218 bursts were rejected because *minpks* or *maxpks* was equal to zero; the rest (3) of the bursts failed the Doppler frequency least-squares fit.

As before, another way of looking at the effect of the criterion of the number of bad burst rejections on the number of good measurements is shown in figure 32 where the individual burst Doppler frequencies are plotted as a function of $SNR_{normalized}$. Again, two cases are shown: *n*bad = 100 (all the coincident bursts are kept) and *n*bad = 0 (only the best bursts are kept). The range of frequency shown in figure 32 is similar to the range shown for the cascade data (fig. 24). What is obvious is that there are not a lot of low $SNR_{normalized}$ bursts with a lot of scatter, as seen for the cascade data. For *n*bad = 0 (in black), the frequency scatter is further reduced and all the lower $SNR_{normalized}$ bursts have been rejected. Actually, all the bursts that remain have $SNR_{normalized}$ values greater than 0.7, which is the reason why the turbulence, frequency, and number of good measurements are constant in the previously shown calibration nozzle exit results (figs. 25 to 28).

Two reasons why the calibration nozzle exit Doppler signals are better as compared with the cascade inlet measurements are (1) better and smaller seed particle distribution and (2) less electronic noise pickup in the cables connecting the photodetectors to the digitizer boards in the computer. The apparently smaller sized seed particles obtained in the flow calibration nozzle tests were discussed previously in the section Laser Anemometer System. This resulted because the seed was injected upstream of a fine wire mesh at the nozzle inlet. The electronic noise was decreased in the calibration nozzle exit tests by moving the computer close to the laser anemometer system and controlling the data acquisition remotely. The result of both of these changes was an increase in the quality of the Doppler signals. This change can be seen in the first and last good burst coincidence data for the calibration nozzle jet shown in figures 33 and 34, respectively.

These results show that there is much less zero-level noise in the calibration nozzle exit Doppler signal than in the cascade inlet data (e.g., see figs. 13 and 16). Also, the near-zero values for *pkmax*(*nl*) result in the normalized SNRs being near 1, indicating very good bursts.

Summary of Results

A laser anemometer (LA) system was used to make two independent measurements from the same seed particle passing through the probe volume of the flow frequencies (equivalent to velocities). The light scattered by the seed particle produces a Doppler signal, or burst, that is captured by high-speed digitizer boards. The purpose in making two independent measurements was to attempt to reduce or eliminate the contribution of photodetector shot noise on the frequency and subsequently on the turbulence estimate. This goal was accomplished by cross-correlating the two independent frequencies and assuming that the shot noise terms are random and not correlated with

themselves or with frequency. Measurements were obtained at the inlet of an annular cascade operating at transonic flow conditions (the cascade inlet flow being subsonic) and at the exit of a flow calibration nozzle. The nozzle exit flow frequency was set to be approximately the same as the cascade inlet flow frequency.

There was no preconditioning of the Doppler signal from the photodetector so that the captured signal contained the pedestal or dc component of the Doppler burst. One observation made relatively early on was that the quality of the individual bursts varied widely, ranging from very bad to very good. Without eliminating the bad bursts, no calculation procedure would give acceptable turbulence estimates. The results of this investigation are as follows:

1. A calculation method was developed to estimate turbulence levels occurring in low turbulent flows. The first step was to determine the good local peaks of the Doppler burst and to reject any bursts with obviously false peaks. Once this was accomplished, Doppler burst symmetry conditions based on the local peak determination were then used to reject bursts without the selected symmetry requirements. Twelve goodness criteria based on local peak and peak symmetry tests were presented; these criteria tended to throw away many more bursts than were kept. With these goodness criteria satisfied, acceptable low-turbulence-level estimates could be made. Some of these tests are specific to the LA optical design used in this experiment but can be modified easily for other LA systems. All the goodness criteria defined herein are independent of frequency.

2. A normalized signal-to-noise ratio ($SNR_{\text{normalized}}$) was defined and tended to allow smaller seed particles to better compete with the larger ones. Although the usual SNR definition was shown to possibly result in larger SNRs for larger seed particles, larger particles might not follow the turbulent fluctuations as well as smaller ones. Therefore, SNR might not be the best quantity to use in determining the goodness of the bursts.

3. The cross-correlated turbulence estimates were always lower than the noncorrelated turbulence estimates. This result tends to support the claim that this cross-correlated method reduced or eliminated the effect of photodetector shot noise on the turbulence determination.

4. The turbulence estimates agreed reasonably well with independent hot-wire measurements. The best agreement was with the cross-correlated turbulence estimates. The small effect of $SNR_{\text{normalized}}$ on the turbulence resulted from the fact that most, if not all, the bursts with a lower $SNR_{\text{normalized}}$ were rejected by the local peak and burst symmetry tests.

5. The turbulence estimation method can be used to give near-real-time results. For example, a typical data subset of 3000 bursts requires about 30 s to process for two $SNR_{\text{normalized}}$, one being zero and the other user defined (e.g., 0.4). A Dell Precision 420 computer with dual Pentium III processors (800 MHz) was used to process the data; the execution times might be different for other computer systems.

6. The frequency estimates were essentially independent of $SNR_{\text{normalized}}$. This result agreed with the theoretical predicted behavior that the frequency is not affected by photodetector shot noise.

7. The quality of the Doppler signals obtained in the calibration nozzle exit flow tests was improved by two means: (1) injecting the seed upstream of a fine wire mesh at the nozzle inlet so that smaller size particles resulted and (2) decreasing the electronic noise in the connecting cables by moving the computer close to the laser anemometer system and controlling the data acquisition remotely.

Glenn Research Center
National Aeronautics and Space Administration
Cleveland, Ohio, April 6, 2004

Figure 1.—Core turbine stator annular cascade and laser anemometer.

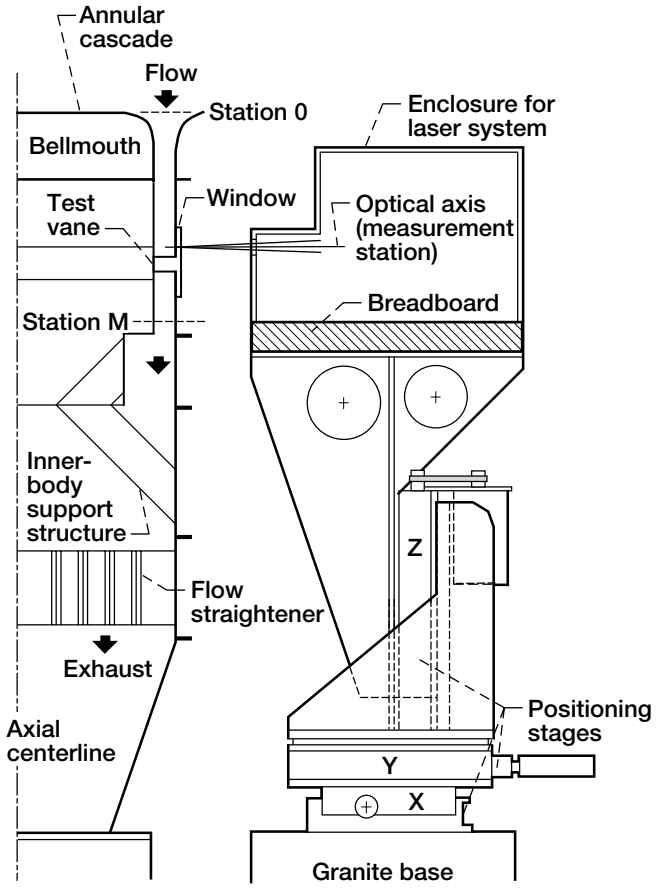

Figure 2.—Cross-sectional view of core turbine stator cascade and laser positioning system.

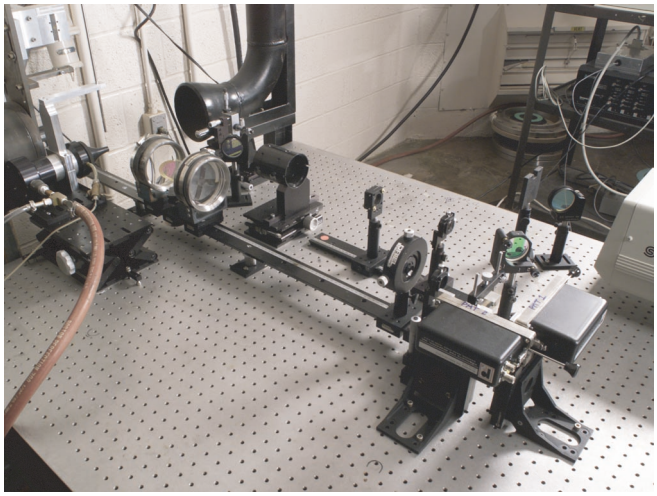

Figure 3.—Flow calibration nozzle and laser anemometer.

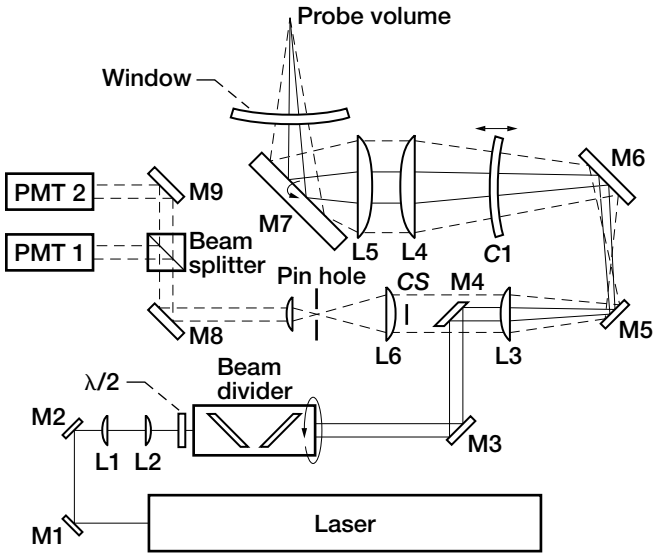

Figure 4.—Optical configuration of laser anemometer measurement system. *CS*, circular stop (mask).

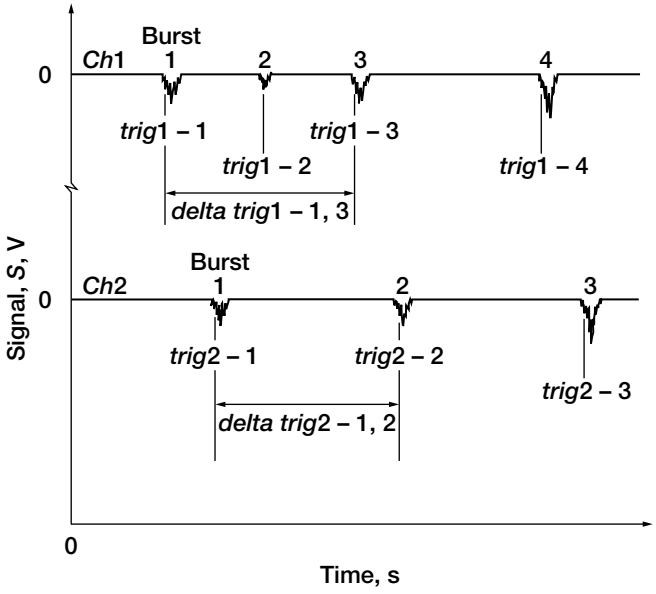

Figure 5.—Two-channel independent Doppler burst records showing nomenclature of burst coincidence determination. *delta trig*1, difference in trigger times for two bursts of *Ch*1; *delta trig*2, difference in trigger times for two bursts of *Ch*2; *trig*1, trigger time for two bursts of *Ch*1; *trig*2, trigger time for two bursts of *Ch*2.

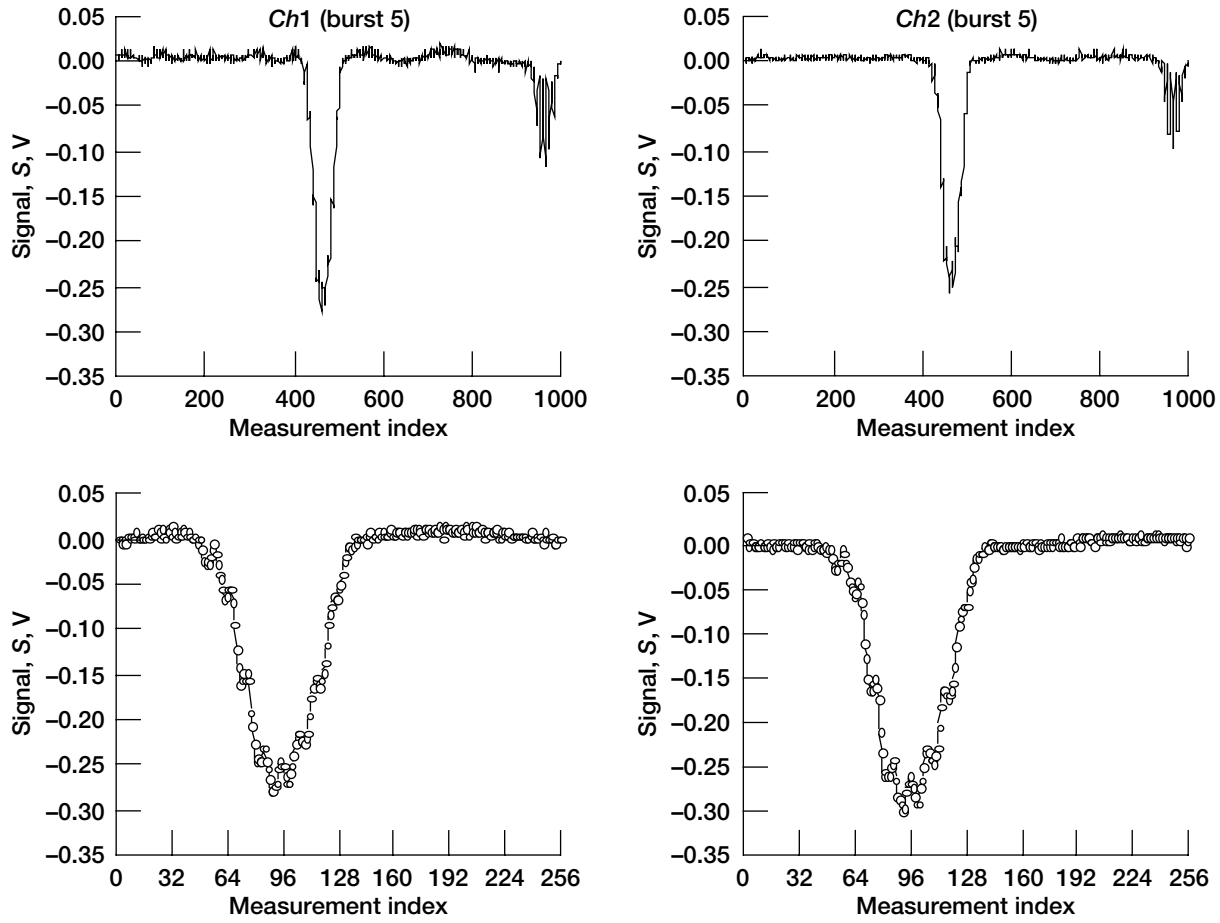

Figure 6.—First burst coincidence for cascade inlet data. Waveform, *wf*, 1.

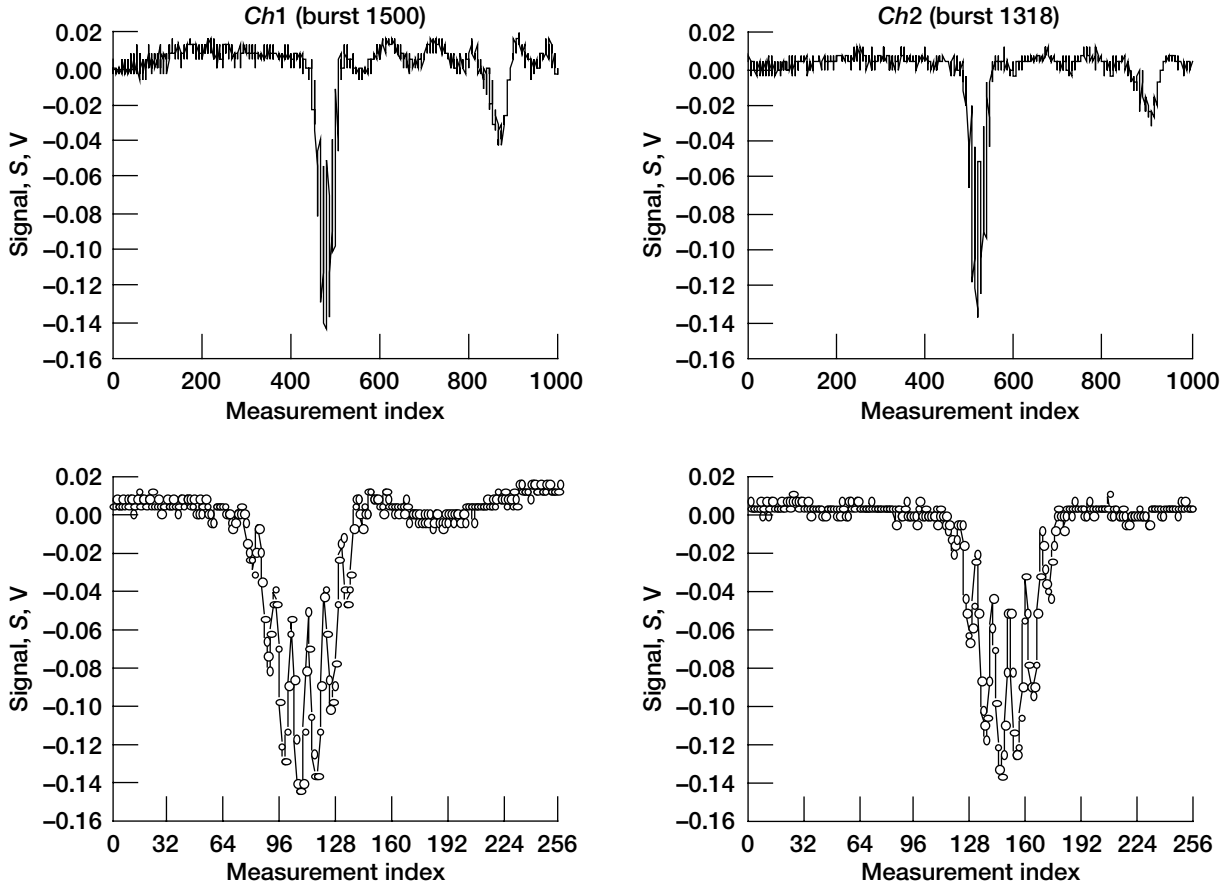

Figure 7.—Last burst coincidence for cascade inlet data. Waveform, *wf*, 1.

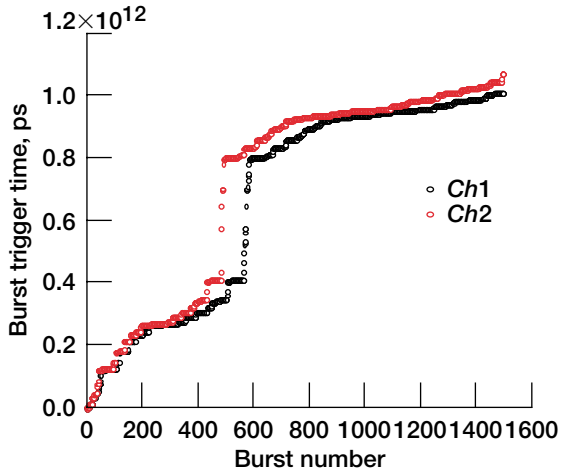

Figure 8.—Burst trigger times versus burst number. Waveform, *wf*, 1.

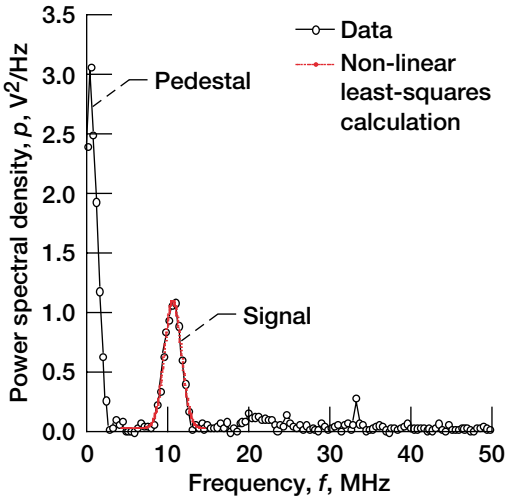

Figure 10.—Typical power spectrum versus frequency from fast Fourier transform for good burst.

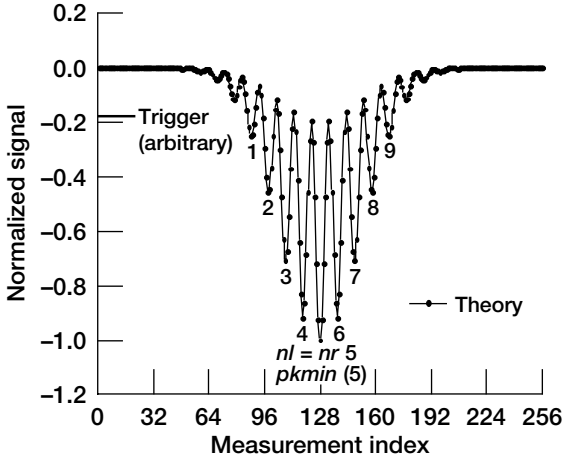

Figure 9.—Theoretical Doppler burst. Visibility, *V*, 2/3; local peak minimum value, *pkmin*, 5; leftmost local peak minimum location, *nl*, = rightmost local peak minimum location, *nr*, 5.

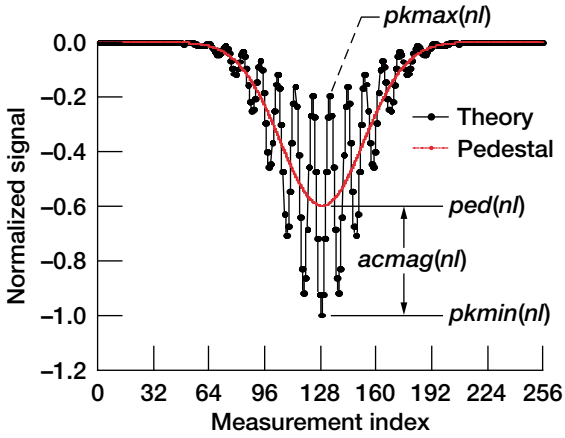

Figure 11.—Nomenclature for estimating signal-to-noise ratio from burst. *acmag*(*nl*), ac magnitude at leftmost local peak minimum; *ped*(*nl*), peak pedestal value; *pkmax*(*nl*), leftmost local peak maximum value; *pkmin*(*nl*), leftmost local peak minimum value.

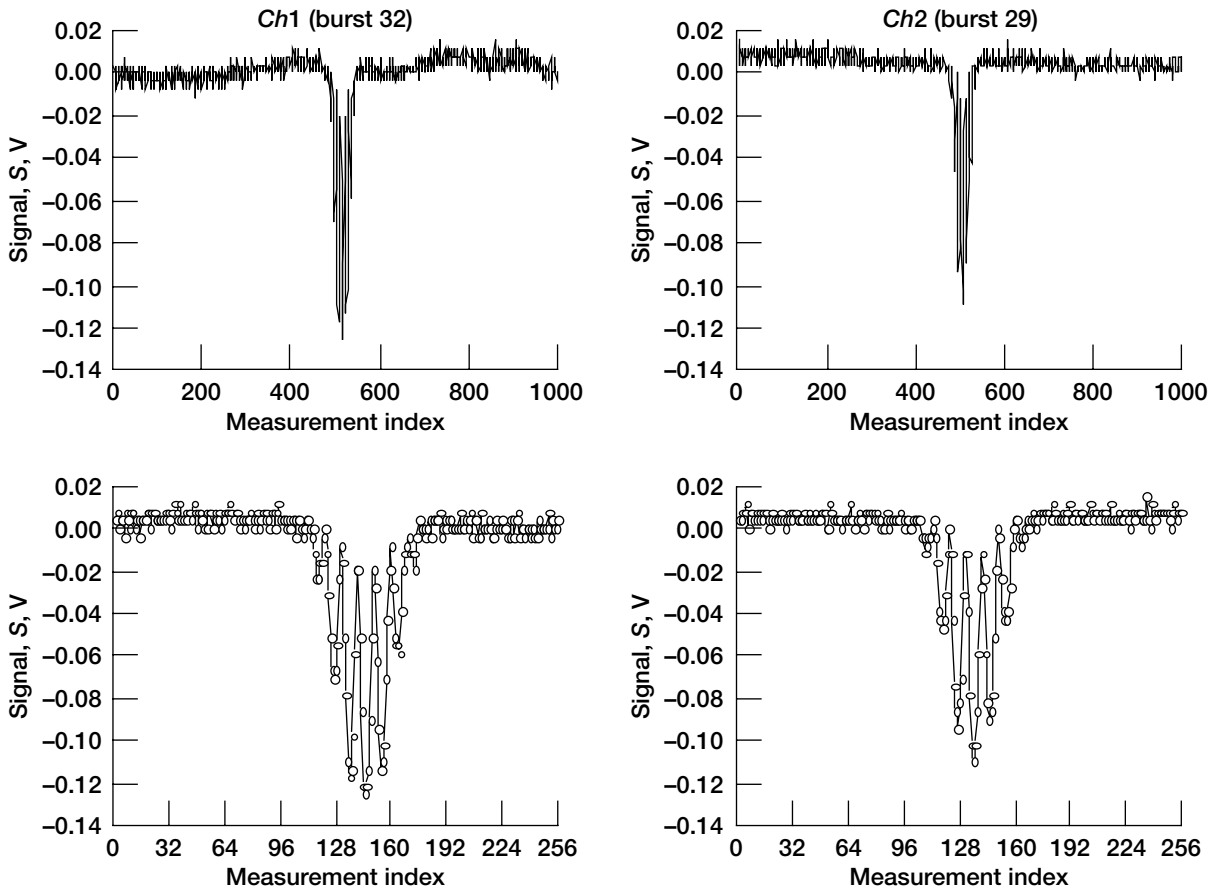

Figure 12.—First good burst coincidence for cascade inlet data. Waveform, *wf*, 1.

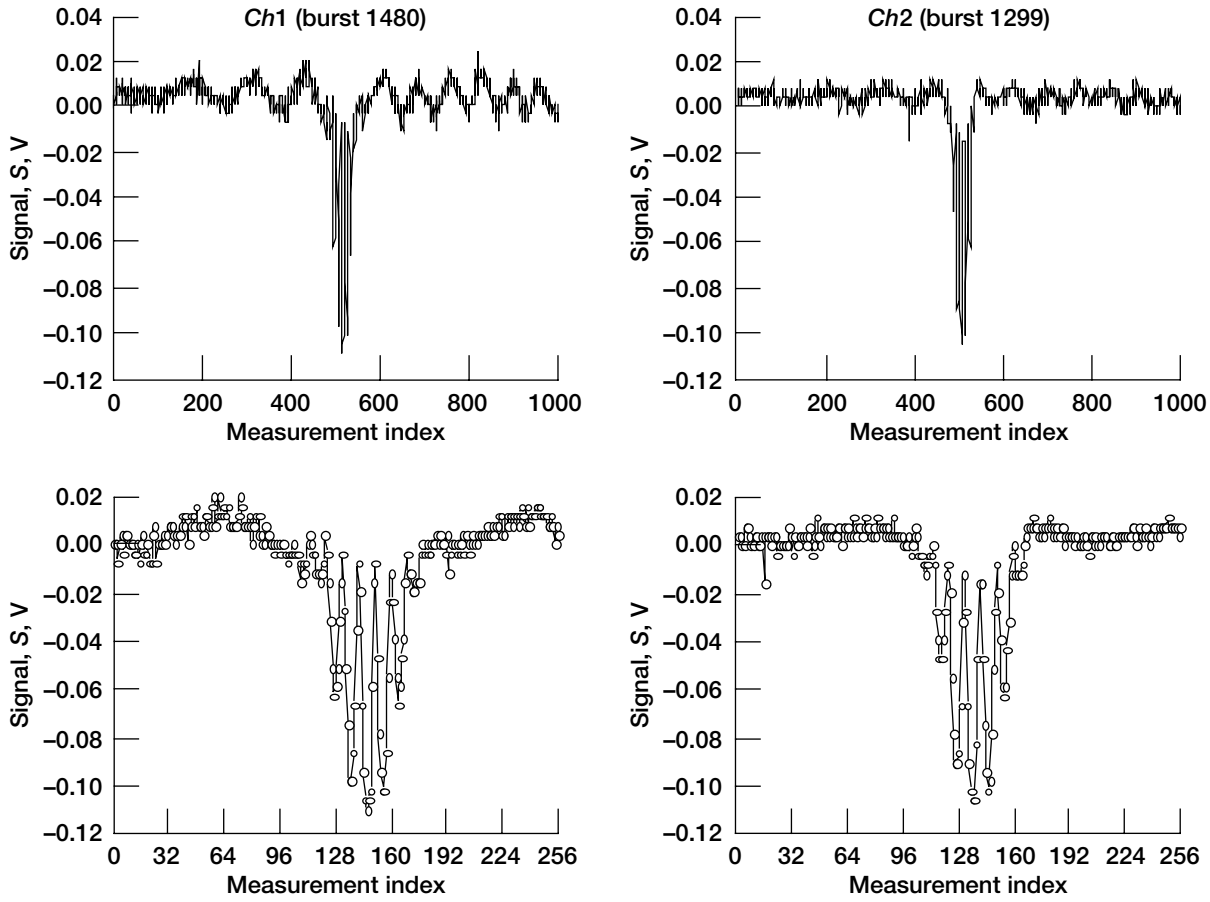

Figure 13.—Last good burst coincidence for cascade inlet data. Waveform, *wf*, 1.

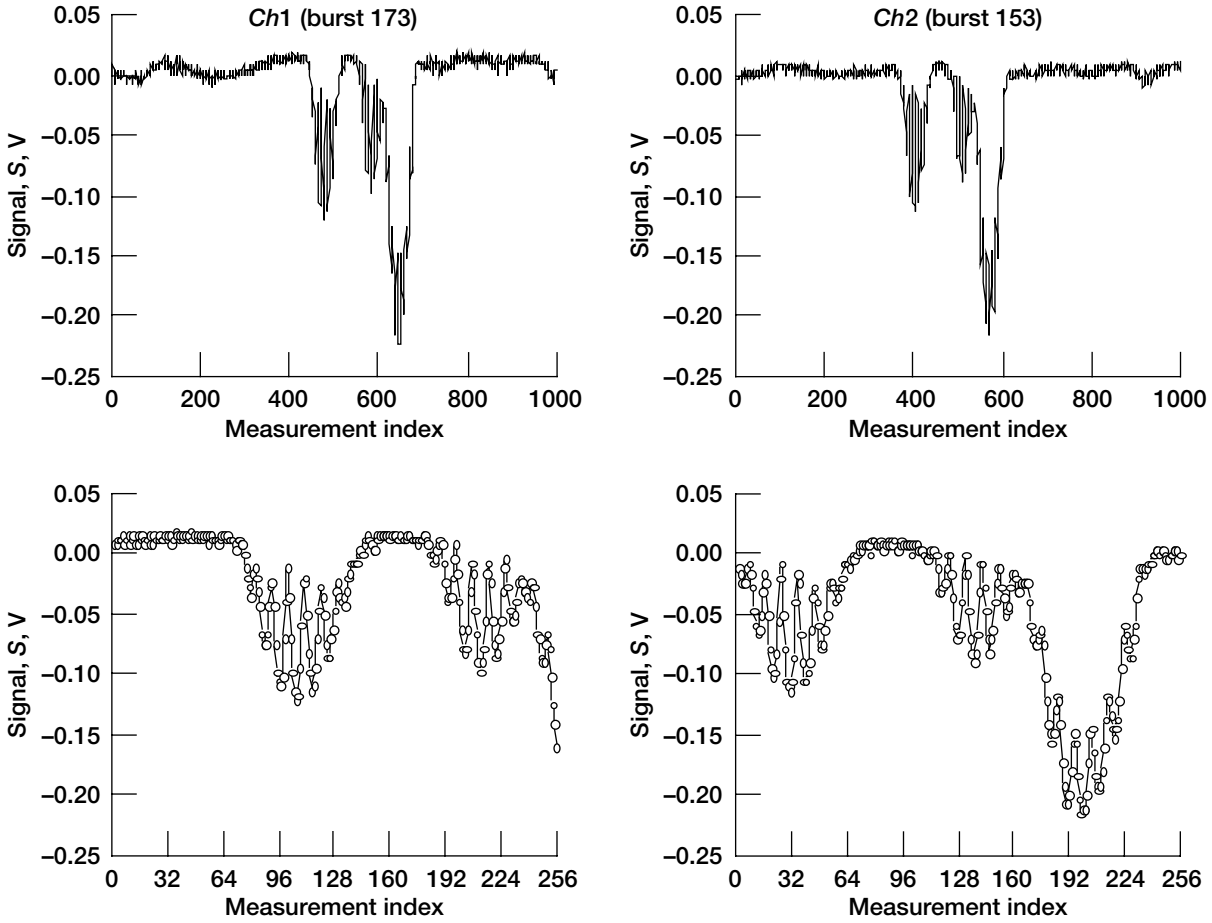

Figure 14.—Bad burst with data point less than local peak minimum for cascade inlet data. Waveform, *wf*, 1.

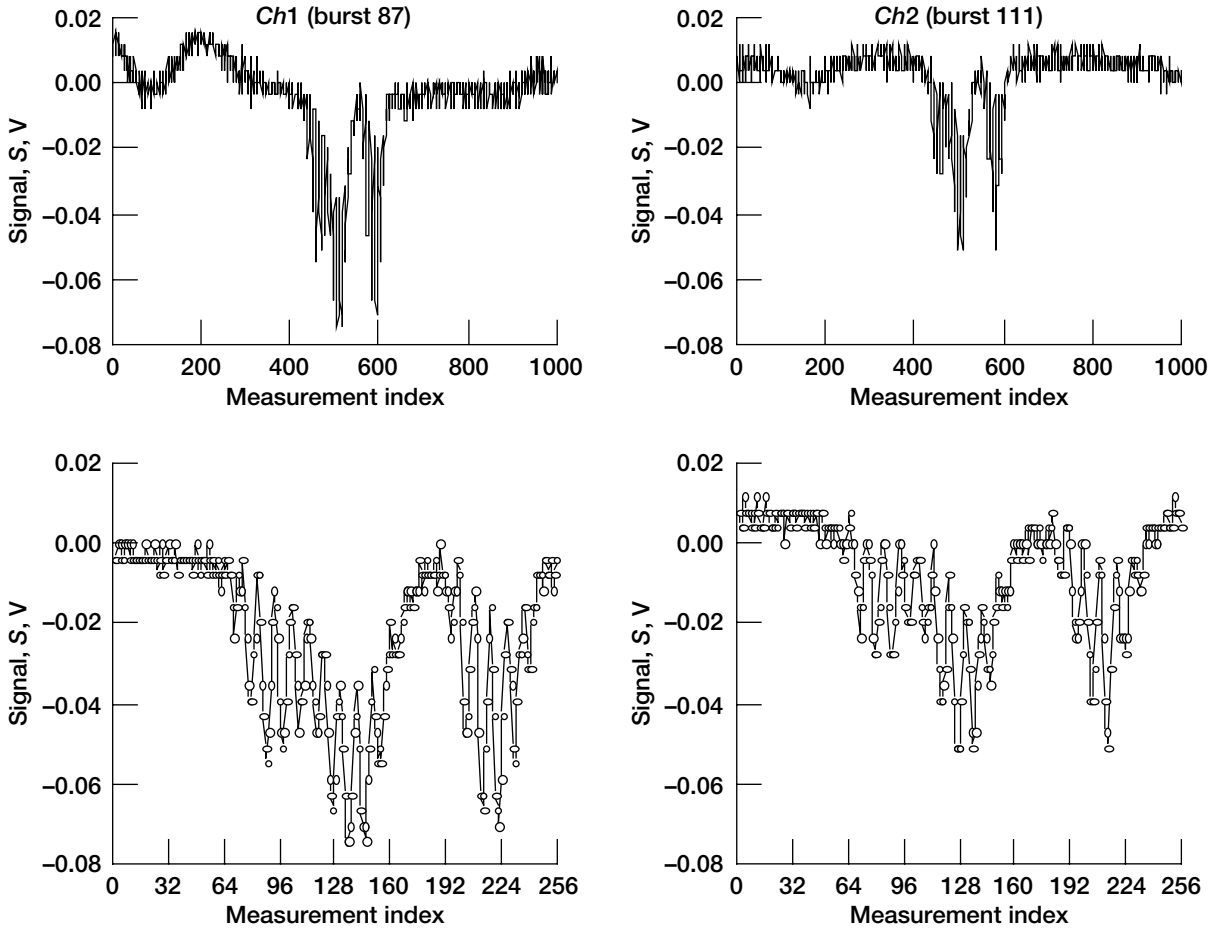

Figure 15.—Bad burst with two equal local peak minimums for cascade inlet data. Waveform, *wf*, 1.

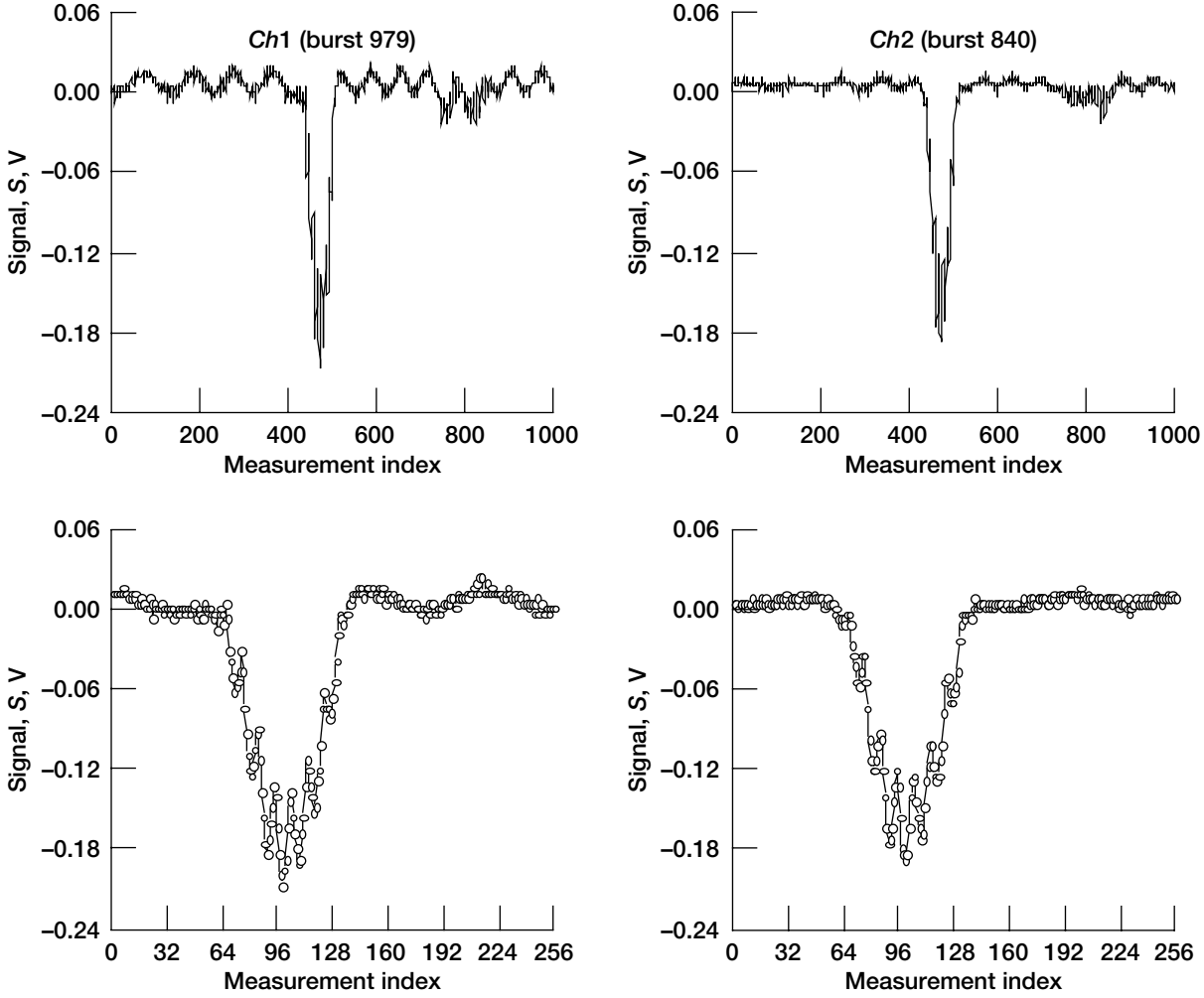

Figure 16.—Good burst with coincidence but low normalized signal-to-noise ratio for cascade inlet data. Waveform, *wf*, 1.

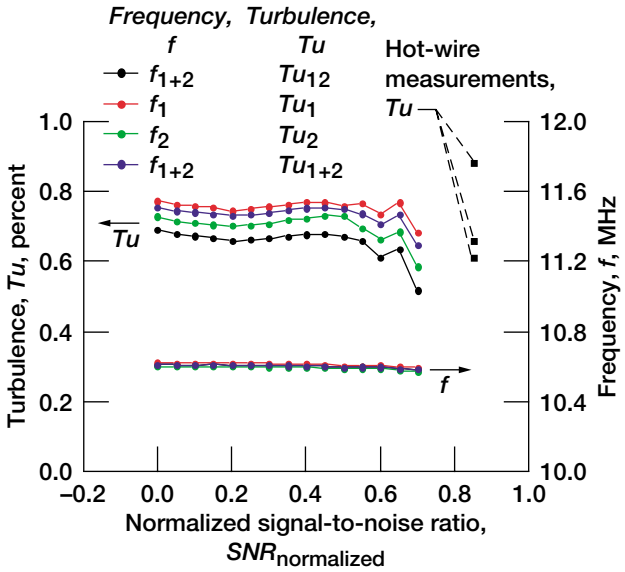

Figure 17.—Turbulence and frequency versus normalized signal-to-noise ratio for cascade inlet data.

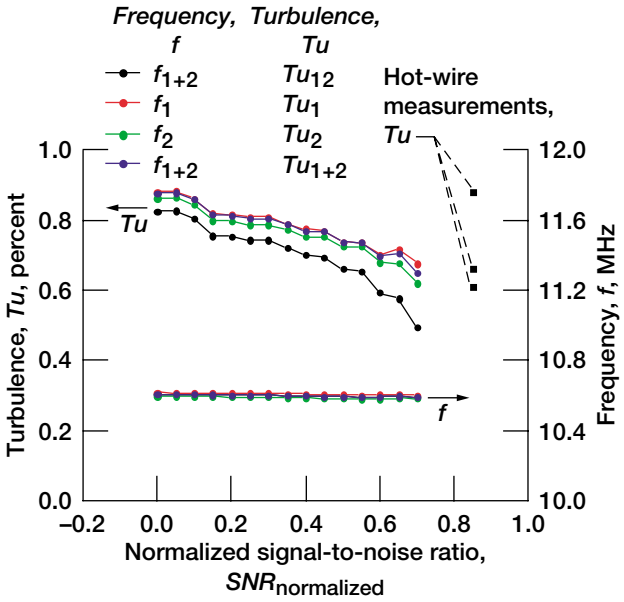

Figure 19.—Turbulence and frequency versus normalized signal-to-noise ratio for cascade inlet data.

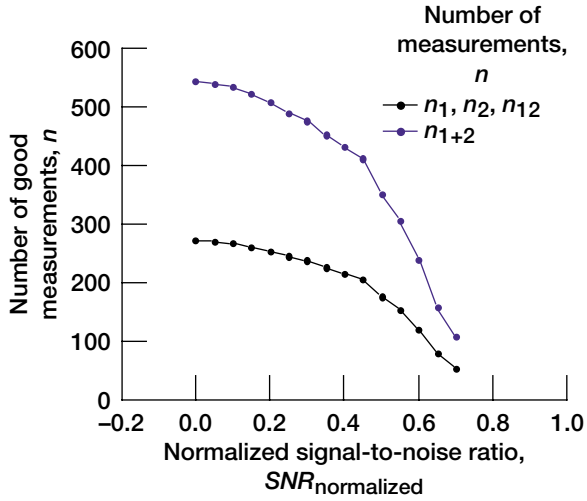

Figure 18.—Number of good measurements versus normalized signal-to-noise ratio for cascade inlet data.

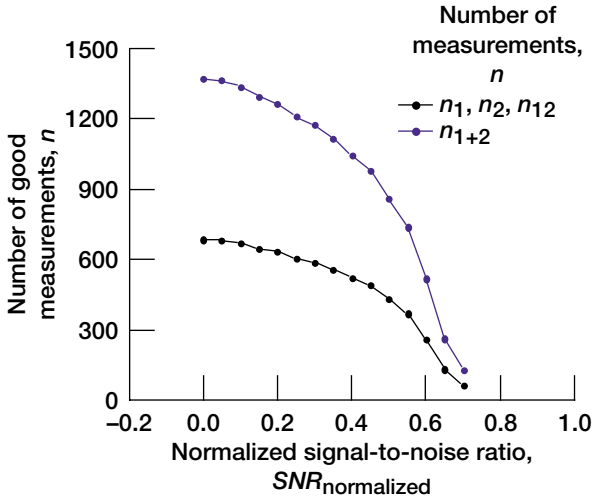

Figure 20.—Number of good measurements versus normalized signal-to-noise ratio for cascade inlet data.

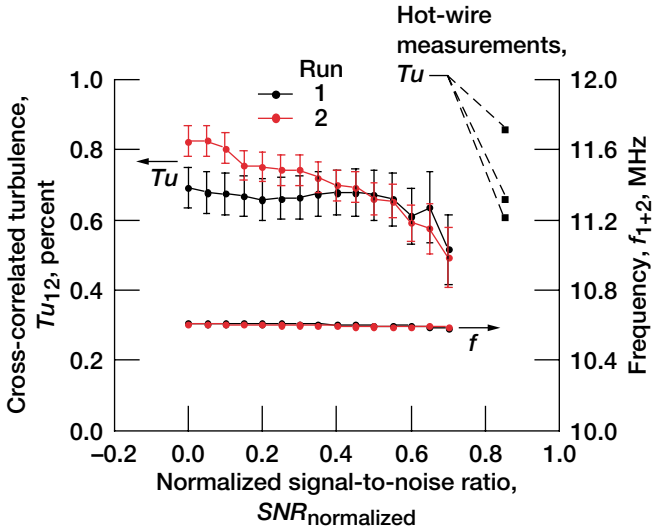

Figure 21.—Comparison of cross-correlated turbulence and frequency for cascade inlet data.

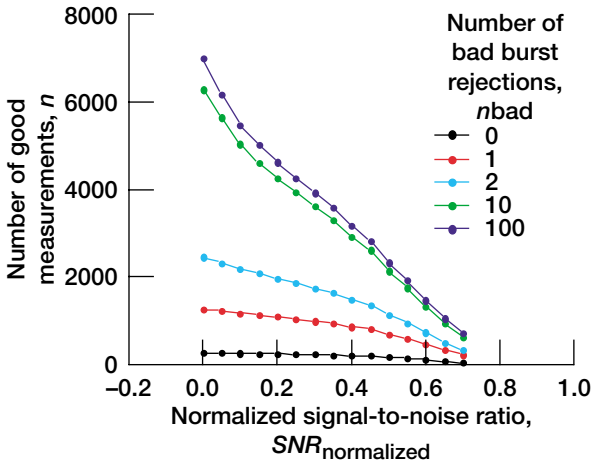

Figure 23.—Effect of number of bad burst rejections, *n*bad, on number of good measurements for cascade inlet data.

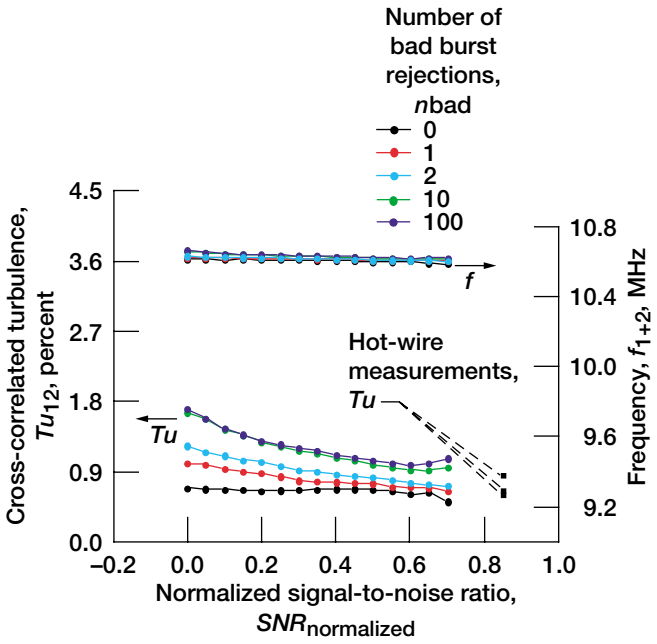

Figure 22.—Effect of number of bad burst rejections, *n*bad, on cross-correlated turbulence and frequency for cascade inlet data.

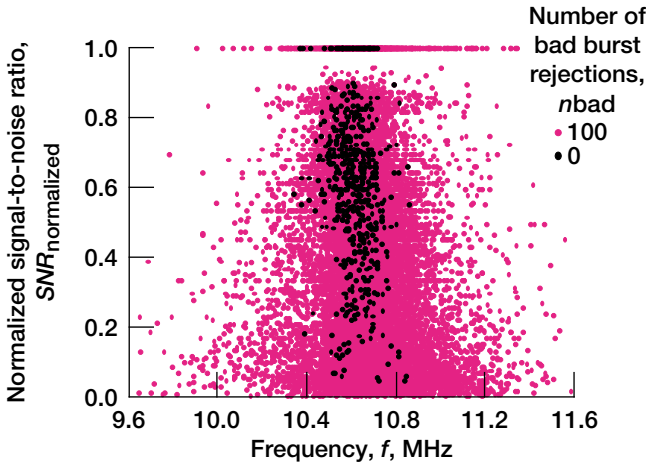

Figure 24.—Individual frequency measurements versus normalized signal-to-noise ratio for cascade inlet data.

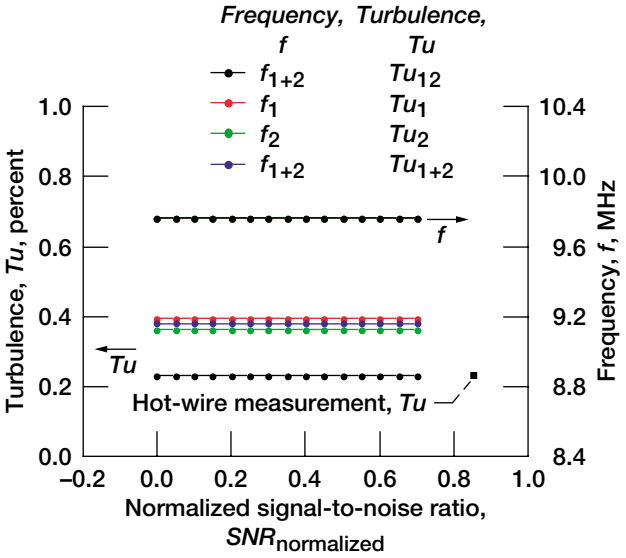

Figure 25.—Turbulence and frequency versus normalized signal-to-noise ratio for nozzle jet exit data.

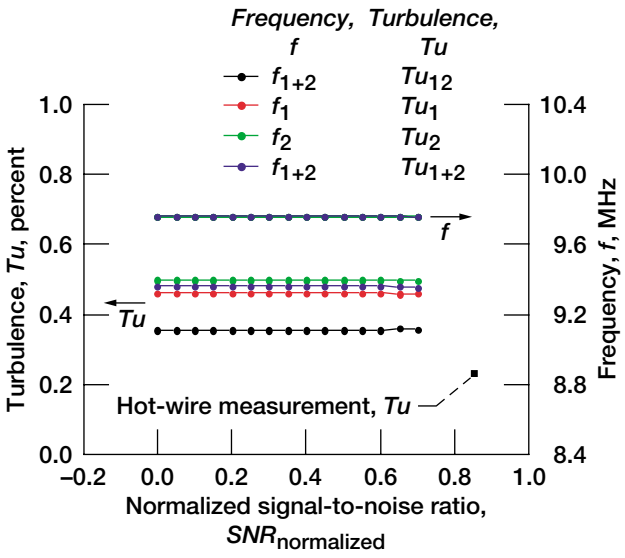

Figure 27.—Turbulence and frequency versus normalized signal-to-noise ratio for nozzle jet exit data.

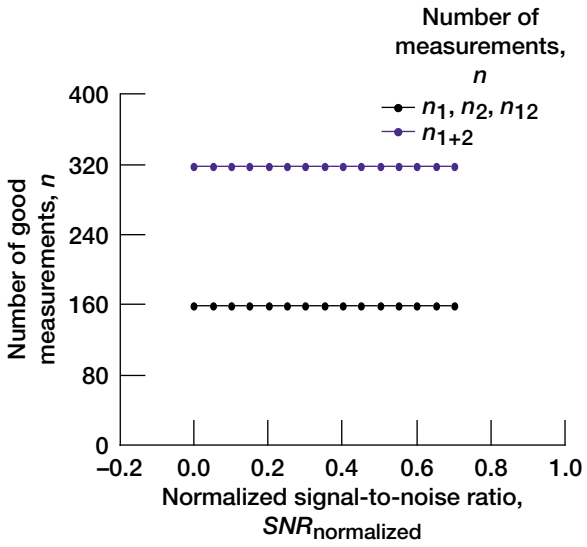

Figure 26.—Number of good measurements versus normalized signal-to-noise ratio for nozzle jet exit data.

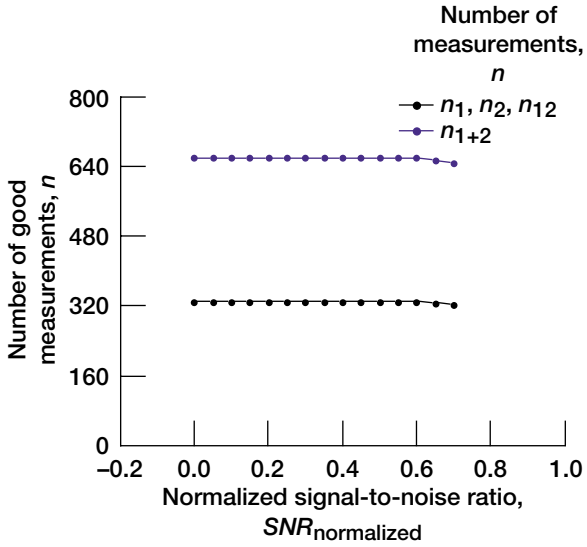

Figure 28.—Number of good measurements versus normalized signal-to-noise ratio for nozzle jet exit data.

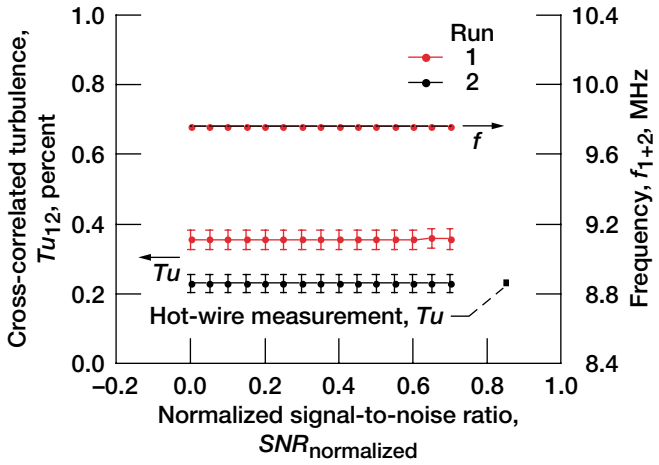

Figure 29.—Comparison of cross-correlated turbulence and frequency for nozzle jet exit data.

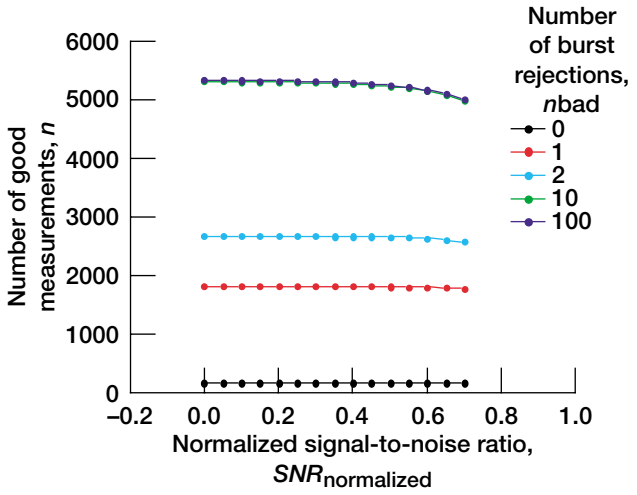

Figure 31.—Effect of number of bad burst rejections, *n*bad, on number of good measurements for nozzle jet exit data.

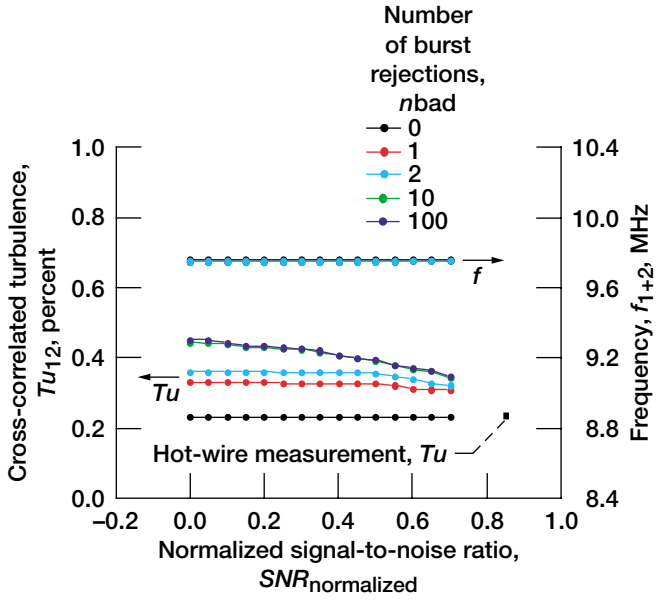

Figure 30.—Effect of number of bad burst rejections, *n*bad, on cross-correlated turbulence and frequency for nozzle jet exit data.

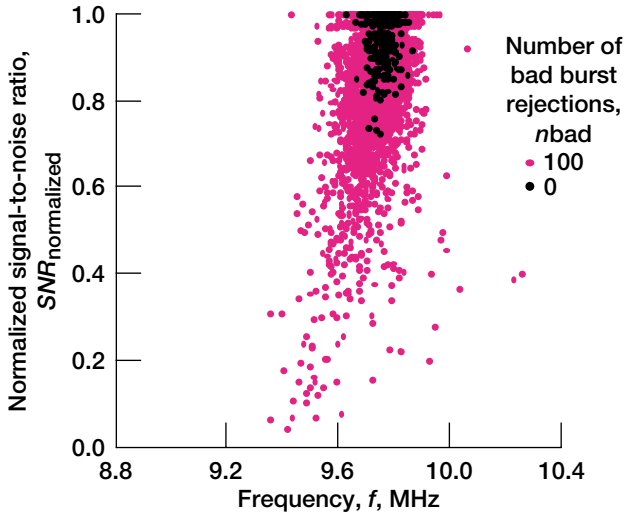

Figure 32.—Individual frequency measurements versus normalized signal-to-noise ratio for nozzle jet exit data.

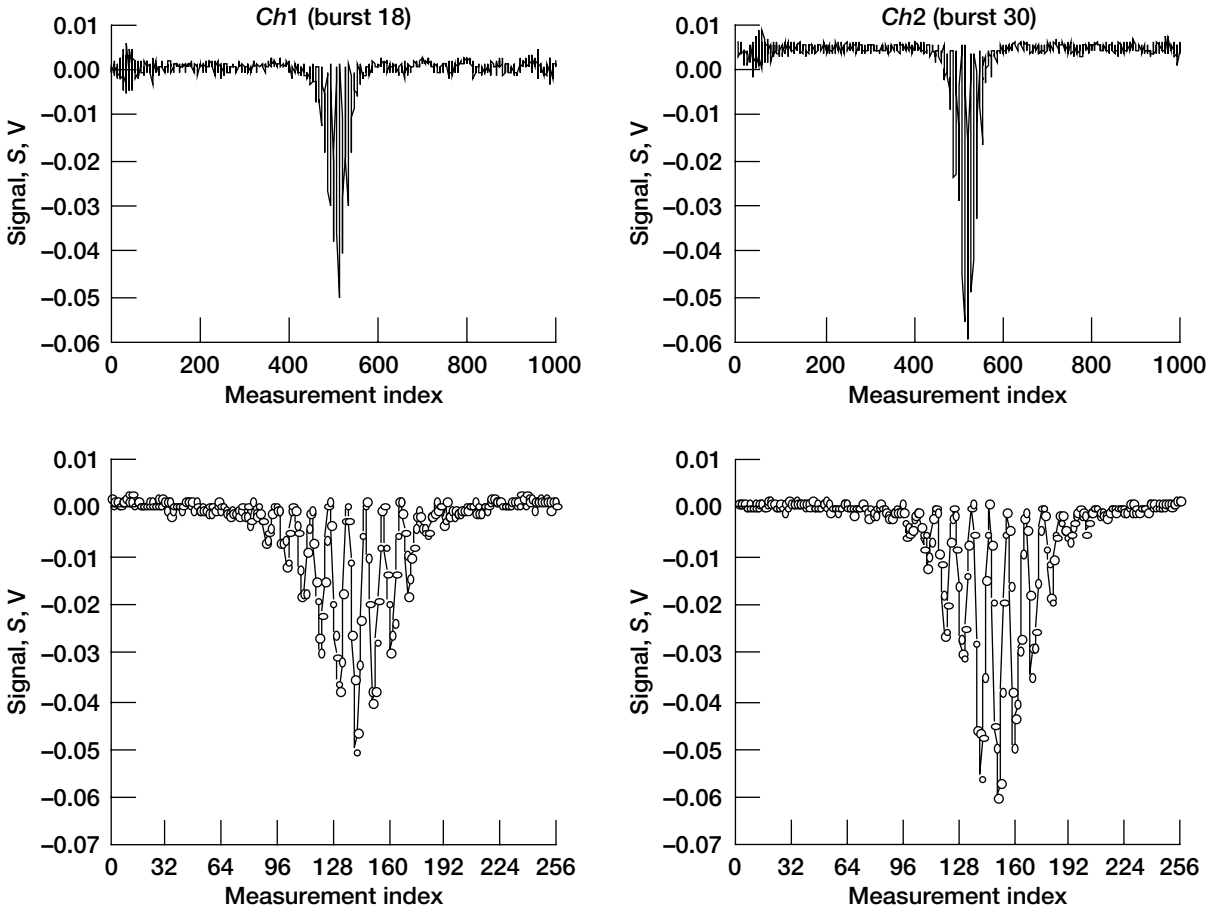

Figure 33.—First good burst coincidence for nozzle jet exit data. Waveform, *wf*, 1.

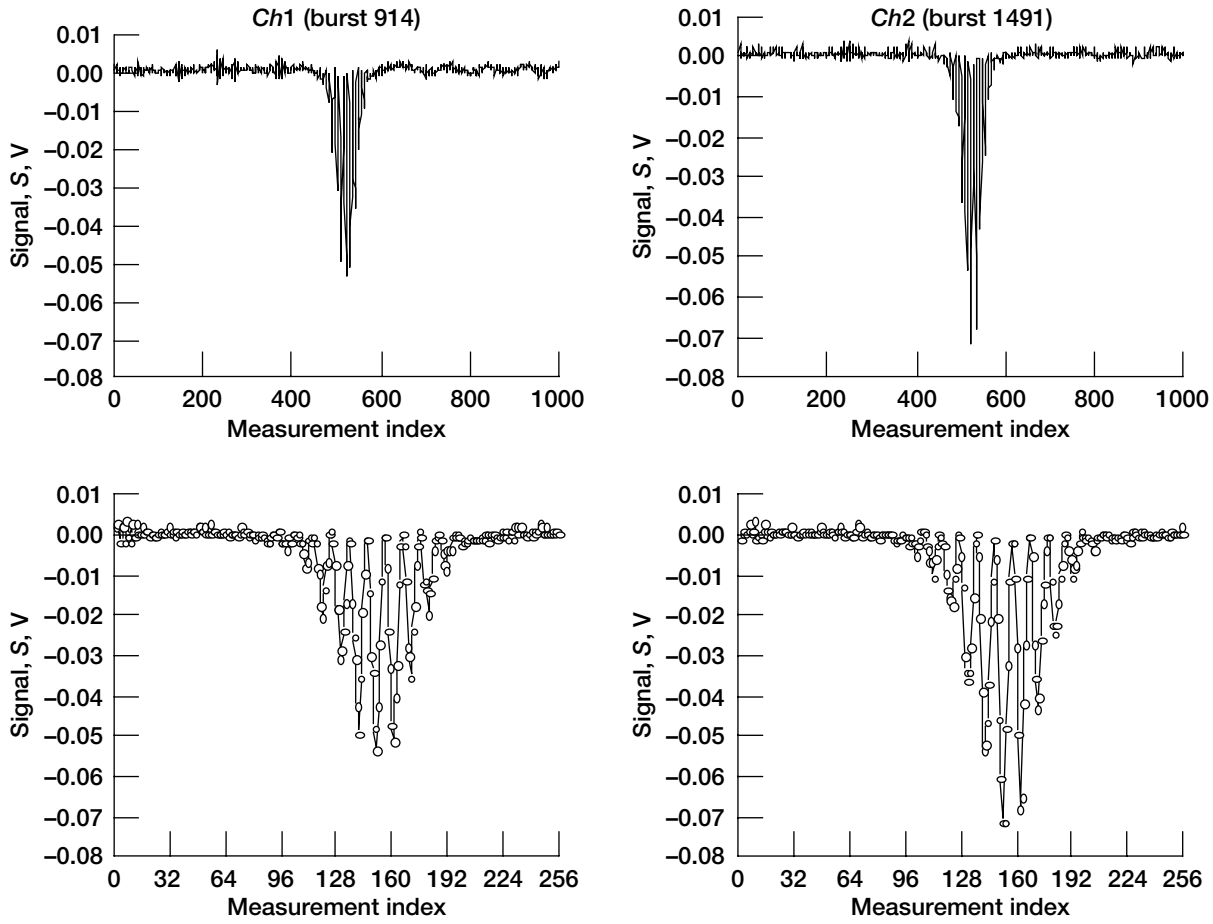

Figure 34.—Last good burst coincidence for nozzle jet exit data. Waveform, *wf*, 1.

Appendix A
Symbols

acmag	*pkmin* – *ped*
*a*1	Gaussian function peak value location (Doppler frequency), MHz
*a*2	Gaussian function half-width, MHz
*a*3	Gaussian function peak value
*a*4	noise term in least-squares model function
*Ch*1	channel 1 (digitizer board 1)
*Ch*2	channel 2 (digitizer board 2)
*c*1,*c*2	constants
*delta trig*1	difference in trigger times for two bursts of *Ch*1
*delta trig*2	difference in trigger times for two bursts of *Ch*2
e_{noise}	random shot noise component of frequency measurement, MHz
f	frequency, MHz
m	*pkmin* index
maxpks	number of local peak maximums
minpks	number of local peak minimums
N	shot noise power, V
n	number of measurements
*n*bad	number of bad burst rejections
nl	leftmost local peak minimum location
nr	rightmost local peak minimum location
p	power spectral density, V^2/Hz
ped	pedestal value
pkmax	local peak maximum value
pkmin	local peak minimum value
S	signal power, V
SNR	signal-to-noise ratio
*trig*1	trigger time for two bursts of *Ch*1
*trig*2	trigger time for two bursts of *Ch*2
Tu	turbulence, percent
V	visibility of burst
wf	waveform; Acqiris nomenclature for single triggered signal (or burst) or complete set of acquired triggered bursts in sequence acquisition mode (typically 1500); complete typical data run consists of 6 waveforms per board

Subscripts:

i	digitizer board index (1 or 2)
j	measurement number index (1 to *n*)
l	lower
maxV	value at maximum visibility of 1
noise	shot noise
normalized	normalized value
Tu_{12}	cross-correlated turbulence
u	upper
1	channel 1
2	channel 2
12	cross-correlated values of *Ch*1 and *Ch*2 measurements

Superscripts:

—	mean value

Appendix B
Signal-to-Noise-Ratio Approximation

This appendix describes a method for estimating the SNR from a given seed particle Doppler burst. The calculations are performed at the peak amplitude *pkmin*(*nl*) and only shot noise generated in the photodetector by light scattered from the seed particles is considered. The SNR value is estimated using the underlying ideas presented in reference 9.

The peak signal power *S*(*nl*) is given by (see fig. 11 for nomenclature)

$$S(nl) = \frac{1}{2} acmag^2(nl) = \frac{1}{2} \frac{acmag^2(nl)}{ped^2(nl)} ped^2(nl)$$

$$= \frac{1}{2} V^2(nl) ped^2(nl) \qquad (8)$$

Where *acmag* is *pkmin* − *ped*. The peak pedestal value *ped*(*nl*) and peak visibility *V*(*nl*) are

$$ped(nl) = \frac{1}{2}\left[pkmin(nl) + pkmax(nl)\right] \qquad (9\,\text{a})$$

and

$$V(nl) = \frac{acmag(nl)}{ped(nl)} = \frac{\left[pkmin(nl) - ped(nl)\right]}{ped(nl)} \qquad (9\,\text{b})$$

$$V(nl) = \frac{\left[pkmin(nl) - pkmax(nl)\right]}{\left[pkmin(nl) + pkmax(nl)\right]} \qquad (10)$$

The peak shot noise power *N*(*nl*) is given by

$$N(nl) = c1\, ped(nl) \qquad (11)$$

The peak signal-to-noise ratio *SNR*(*nl*) is therefore

$$SNR(nl) = \frac{S(nl)}{N(nl)} = \frac{1}{2} c1 V^2(nl) ped(nl)$$

$$SNR(nl) = c2 \frac{\left[pkmin(nl) - pkmax(nl)\right]^2}{\left[pkmin(nl) + pkmax(nl)\right]} \qquad (12)$$

If *pkmax*(*nl*) = 0, the visibility *V*(*nl*) and the *SNR*(*nl*) are

$$V(nl) = 1 \text{ and } \quad SNR(nl)_{maxV} = c2\, pkmin(nl) \qquad (13)$$

A maximum visibility of 1 indicates the probability of a very good burst. Equation (13) indicates that bursts with larger *pkmin*(*nl*) values are better than bursts with smaller *pkmin*(*nl*) values, since larger *pkmin*(*nl*) bursts give larger $SNR_{max\text{V}}$ values. This fact suggests that larger particles result in better bursts because they scatter more light and give larger *pkmin*(*nl*) values. However, larger particles may not follow the flow fluctuations as well as smaller particles, so turbulence estimates based on SNR may not be the best criterion to use. Therefore, a normalized $SNR(nl)_{\text{normalized}}$ was defined herein as

$$SNR(nl)_{\text{normalized}} = \frac{SNR(nl)}{SNR(nl)_{maxV}}$$

$$SNR(nl)_{\text{normalized}} = \frac{\left[pkmin(nl) - pkmax(nl)\right]^2}{pkmin(nl)\left[pkmin(nl) + pkmax(nl)\right]} \qquad (14)$$

This definition of a normalized SNR allows smaller particles to compete with larger particles on an equal basis. Note that if *pkmax*(*nl*) = 0, $SNR(nl)_{\text{normalized}} = 1$, a very good burst (visibility V(*nl*) = 1). Also, if *pkmax*(*nl*) = *pkmin*(*nl*), $SNR(nl)_{\text{normalized}} = 0$, a very bad burst (visibility V(*nl*) = 0).

Appendix C
Cross-Correlated Turbulence Estimate

This appendix describes the method of estimating the turbulence from the cross-correlation of the two independent frequency measurements obtained from the same seed particle passing through the probe volume (i.e., bursts that are coincident, as discussed in the section Dual-Channel Burst Coincidence Determination). As described in reference 3, this method should remove or reduce photodetector shot noise. As evidence, consider that the measured frequency containing shot noise $f_{i,j,\text{noise}}$ can be written as the sum of the true frequency $f_{i,j}$, and a shot noise term $e_{i,j,\text{noise}}$:

$$\begin{aligned} f_{i,j,\text{noise}} &= f_{i,j} + e_{i,j,\text{noise}} \\ i &= 1,2\ (Ch1, Ch2) \\ j &= 1 - n \end{aligned} \qquad (15)$$

The average frequency $\overline{f_{1+2}}$ is

$$\overline{f_{1+2}} = \frac{1}{2n}\sum_{j=1}^{n}\left(f_{1,j} + e_{1,j,\text{noise}} + f_{2,j} + e_{2,j,\text{noise}}\right) \quad (16)$$

Since the two shot noise terms from the photodetectors are considered random and uncorrelated, the sums containing these terms should approach zero if enough measurements are taken:

$$\overline{f_{1+2}} = \frac{1}{2n}\sum_{j=1}^{n}\left(f_{1,j} + f_{2,j}\right) = \frac{1}{2}\left(\overline{f_1} + \overline{f_2}\right)$$

$$\overline{f_1} = \frac{1}{n}\sum_{j=1}^{n} f_{1,j} \quad \text{and} \quad \overline{f_2} = \frac{1}{n}\sum_{j=1}^{n} f_{2,j} \qquad (17)$$

The average frequency $\overline{f_{1+2}}$ is therefore independent of photodetector shot noise.

The cross-correlated turbulence Tu_{12} is calculated from

$$Tu_{12}^2 = \frac{1}{n}\sum_{j=1}^{n}\left[\ \overline{f_{1+2}} - \left(f_{1,j} + e_{1,j}\right)\right]\left[\ \overline{f_{1+2}} - \left(f_{2,j} + e_{2,j}\right)\right]$$

$$Tu_{12}^2 = \frac{1}{n}\sum_{j=1}^{n}\left[\overline{f_{1+2}}^2 - \overline{f_{1+2}}\left(f_{1,j} + f_{2,j} + e_{1,j} + e_{2,j}\right)\right.$$

$$\left. + \left(f_{1,j} + e_{1,j}\right)\left(f_{2,j} + e_{2,j}\right)\right] \qquad (18)$$

The two shot noise terms are also considered to be uncorrelated to frequency or to themselves. So, terms like f_1e_1, f_1e_2, e_1e_2, and so forth tend to go to zero if enough measurements are taken. Equation (18) then becomes (after using the definitions in eq. (17))

$$Tu_{12}^2 = \frac{1}{n}\sum_{j=1}^{n}\left[\overline{f_{1+2}}^2 - \overline{f_{1+2}}\left(f_{1,j} + f_{2,j}\right) + f_{1,j}f_{2,j}\right]$$

$$= \frac{1}{n}\sum_{j=1}^{n} f_{1,j}f_{2,j} - \overline{f_{1+2}}^2 \qquad (19)$$

Defining,

$$\overline{f_1 f_2} = \frac{1}{n}\sum_{j=1}^{n} f_{1,j}f_{2,j} \qquad (20)$$

gives, finally, Tu_{12} as a percent:

$$Tu_{12} = 100.0\frac{\sqrt{\overline{f_1 f_2} - \overline{f_{1+2}}^2}}{\overline{f_{1+2}}} \qquad (21)$$

An estimate of the uncertainty of the turbulence based on a 95-percent confidence level standard deviation (ref. 10) is given by

$$sd_{Tu_{12}} = Tu_{12}\sqrt{\frac{2}{n}} \qquad (22)$$

Note that if $\overline{f_1} = \overline{f_2} \equiv \overline{f}$, the turbulence (eq. 21) reverts to its familiar form:

$$Tu_{12} = 100.0\frac{\sqrt{\overline{f^2} - \overline{f}^2}}{\overline{f}} \qquad (23)$$

Similar to the estimate of the average frequency (eq. 17), that of the cross-correlated turbulence Tu_{12} is independent of photodetector shot noise.

The independence of the estimate of cross-correlated turbulence on photodetector shot noise is not the case if only one set of measurements is taken, as seen from equation (18). In this equation, $f_{1,j} = f_{2,j} \equiv f_j$, and $e_{1,j} = e_{2,j} \equiv e_j$, resulting in a square term e_j^2, which is always positive and thus gives a false turbulence estimate. That is,

$$Tu^2 = \frac{1}{n}\sum_{j=1}^{n}\left[\overline{f}^2 - \overline{f}\left(2f_j + 2e_j\right) + \left(f_j + e_j\right)^2\right]$$

$$= \frac{1}{n}\sum_{j=1}^{n}\left(\overline{f}^2 - 2\overline{f}f_j + f_j^2 + e_j^2\right) \qquad (24)$$

where, as before, the two shot noise terms are considered to be uncorrelated to frequency. Using the definition in equation (17), equation (24) becomes

$$Tu^2 = \overline{f^2} - \overline{f}^2 + e^2 \qquad (25)$$

or as a percent,

$$Tu = 100.0\frac{\sqrt{\overline{f^2} - \overline{f}^2 + e^2}}{\overline{f}} \qquad (26)$$

Because of the e^2 term, the turbulence estimated with a single-channel measurement system (eq. (26)) will always be larger than that obtained by cross-correlation of a two-channel measurement system (eq. (23)).

References

1. Goldman, Louis J.: Laser Anemometer Measurements and Computations for Transonic Flow Conditions in an Annular Cascade of High Turning Core Turbine Vanes. NASA TP–3383, 1993.
2. Tropea, C.: Laser-Doppler Anemometry—Recent Developments and Future Challenges. Meas. Sci. Technol., vol. 6, no. 6, 1995, pp. 605–619.
3. Lau, J.C., et al.: A Note on Turbulence Measurements With a Laser Velocimeter. J. Fluid Mech., vol. 102, 1981, pp. 353–366.
4. Goldman, L.J.; and Seasholtz, R.G.: Laser Anemometer Measurements in an Annular Cascade of Core Turbine Vanes and Comparison With Theory. NASA TP–2018, 1982.
5. acqiris. http://www.acqiris.com/index.html Accessed Jan. 13, 2004.
6. Wolberg, John R.: Prediction Analysis. D. Van Nostrand, Princeton, NJ, 1967.
7. Beck, J.V.; and Arnold, Kenneth J.: Parameter Estimation in Engineering and Science. Wiley, New York, NY, 1977.
8. Press, William H., et al.: Numerical Recipes: The Art of Scientific Computing. Fortran version, Cambridge University Press, Cambridge, NY, 1989.
9. Adrian, R.J.: Estimation of LDA Signal Strength and Signal-to-Noise Ratio. University of Illinois at Urbana-Champaign, TSI Quarterly, 1978, pp. 3–8.
10. Yanta, W.J.: Turbulence Measurements With a Laser Doppler Velocimeter. NOLTR7394, 1973.

REPORT DOCUMENTATION PAGE

Form Approved
OMB No. 0704-0188

1. AGENCY USE ONLY (*Leave blank*)	2. REPORT DATE	3. REPORT TYPE AND DATES COVERED
	September 2004	Technical Paper

4. TITLE AND SUBTITLE

A Method of Estimating Low Turbulence Levels in Near Real Time Using Laser Anemometry

5. FUNDING NUMBERS

WBS–22–714–30–10

6. AUTHOR(S)

Louis J. Goldman and Richard G. Seasholtz

7. PERFORMING ORGANIZATION NAME(S) AND ADDRESS(ES)

National Aeronautics and Space Administration
John H. Glenn Research Center at Lewis Field
Cleveland, Ohio 44135–3191

8. PERFORMING ORGANIZATION REPORT NUMBER

E–14326

9. SPONSORING/MONITORING AGENCY NAME(S) AND ADDRESS(ES)

National Aeronautics and Space Administration
Washington, DC 20546–0001

10. SPONSORING/MONITORING AGENCY REPORT NUMBER

NASA TP—2004-212903

11. SUPPLEMENTARY NOTES

Responsible person, Richard G. Seasholtz, organization code 5520, 216–433–3754.

12a. DISTRIBUTION/AVAILABILITY STATEMENT

Unclassified - Unlimited
Subject Category: 02 Distribution: Standard

Available electronically at http://gltrs.grc.nasa.gov

This publication is available from the NASA Center for AeroSpace Information, 301–621–0390.

12b. DISTRIBUTION CODE

13. ABSTRACT ***(Maximum 200 words)***

Laser anemometry was used to make two independent measurements of the flow velocity by capturing individual Doppler signals with high-speed digitizing boards. The two independent measurements were cross-correlated to reduce the contribution of photo detector shot noise on the frequency determination and subsequently on the turbulence estimate. In addition, criteria were developed to eliminate "bad" Doppler bursts from the data set, which then allowed reasonable low turbulence estimates to be made. The laser anemometer measurements were obtained at the inlet of an annular cascade and at the exit of a flow calibration nozzle and were compared with hot-wire data.

14. SUBJECT TERMS

Turbulence; Low-level turbulence; Flow measurement; Cascade flow; Nozzle flow; Laser anemometers; Laser Doppler velocimeters

15. NUMBER OF PAGES

40

16. PRICE CODE

17. SECURITY CLASSIFICATION OF REPORT	18. SECURITY CLASSIFICATION OF THIS PAGE	19. SECURITY CLASSIFICATION OF ABSTRACT	20. LIMITATION OF ABSTRACT
Unclassified	Unclassified	Unclassified	